

# Solar Thermochemical Conversion of Carbon Dioxide into Fuel via $MnFe_2O_4$ based Two-Step Redox Cycle

Rahul Bhosale (✉ [rahul.bhosale@qu.edu.qa](mailto:rahul.bhosale@qu.edu.qa))

Qatar University <https://orcid.org/0000-0002-2697-8141>

---

## Research Article

**Keywords:** CO<sub>2</sub> splitting, thermodynamic model, solar fuels, gas-to-gas heat recovery

**Posted Date:** February 11th, 2021

**DOI:** <https://doi.org/10.21203/rs.3.rs-166657/v1>

**License:**  This work is licensed under a Creative Commons Attribution 4.0 International License.

[Read Full License](#)

---



43 **ABSTRACT**

44 Thermodynamic efficiency analysis of  $MnFe_2O_4$  based  $CO_2$  splitting (CDS) cycle is reported. HSC  
45 Chemistry software is used for performing the calculations allied with the model developed. By  
46 maintaining the reduction nonstoichiometry equal to 0.1, variations in the thermal energy  
47 required to drive the cycle ( $\dot{Q}_{TC}$ ) and solar-to-fuel energy conversion efficiency ( $\eta_{solar-to-fuel}$ )  
48 as a function of the ratio of the molar flow rate of inert sweep gas ( $\dot{n}_{inert}$ ) to the molar flow rate  
49  $MnFe_2O_4$  ( $\dot{n}_{MnF}$ ), i.e.,  $\dot{n}_{inert}/\dot{n}_{MnF}$ , reduction temperature ( $T_{red}$ ), and gas-to-gas heat recovery  
50 effectiveness ( $\varepsilon_{gg}$ ) are studied. The rise in  $\dot{n}_{inert}/\dot{n}_{MnF}$  is responsible for the decrease in  $T_{red}$ . At  
51  $\varepsilon_{gg} = 0.7$ ,  $\dot{Q}_{TC}$  increases from 176.0 kW to 271.7 kW when  $\dot{n}_{inert}/\dot{n}_{MnF}$  escalates from 10 to 100.  
52 Conversely,  $\eta_{solar-to-fuel}$  reduces from 14.9% to 9.9% due to the similar increment in  
53  $\dot{n}_{inert}/\dot{n}_{MnF}$ . The difference between  $\dot{Q}_{TC}$  at  $\dot{n}_{inert}/\dot{n}_{MnF} = 10$  and 100 decreases from 363.3 kW  
54 to 19.2 kW as  $\varepsilon_{gg}$  rises from 0.0 to 0.9. As  $\dot{Q}_{TC}$  and subsequently  $\dot{Q}_{solar}$  reduces as a function of  
55  $\varepsilon_{gg}$ ,  $\eta_{solar-to-fuel}$  increases noticeably. At  $\varepsilon_{gg}$  equal to 0.9 and  $\dot{n}_{inert}/\dot{n}_{MnF}$  equal to 10 as well  
56 as 20, the maximum  $\eta_{solar-to-fuel}$  equal to 17.5% is realized.

57 Keywords:  $MnFe_2O_4$ ,  $CO_2$  splitting, thermodynamic model, solar fuels, gas-to-gas heat recovery

58

59

60

61

## 62 **1. Introduction**

63 The hazardous effects associated with the incessant emissions of CO<sub>2</sub> can be resolved by using  
64 technologies such as the solar thermochemical CO<sub>2</sub> splitting (CDS) cycle(Bhosale et al. 2019). This  
65 cycle is capable of splitting CO<sub>2</sub> into CO by using solar thermal power. The solar thermochemical  
66 community's final aim is to produce solar syngas by combining CO produced from CDS and H<sub>2</sub>  
67 produced from H<sub>2</sub>O splitting (WS)(Agrafiotis et al. 2015). A variety of fuels can be manufactured  
68 using the solar syngas via the catalytic Fischer Tropsch process.

69 The redox chemistry associated with the metal oxides (MOs) is used for driving the solar  
70 thermochemical cycle. Several MOs redox systems were investigated until now for both CDS and  
71 WS. The list includes ZnO/Zn(Koepf et al. 2016), SnO<sub>2</sub>/SnO/Sn(Abanades et al. 2008),  
72 Fe<sub>3</sub>O<sub>4</sub>/FeO/Fe(Kodama et al. 2006), ferrites(Amar et al. 2015), ceria(Bulfin et al. 2015), doped  
73 ceria(Takalkar et al. 2019), and perovskites(Dey et al. 2015). Among all the above mentioned  
74 MOs, ferrites (which are doped iron oxides) were examined for WS application more than CDS.  
75 The ferrites investigated until now mainly includes NiFe<sub>2</sub>O<sub>4</sub>(Bhosale 2019a), CoFe<sub>2</sub>O<sub>4</sub>(Scheffe et  
76 al. 2010), ZnFe<sub>2</sub>O<sub>4</sub> (Tamura et al. 2001), Sn-ferrite(Bhosale et al. 2011), Mg-ferrite(Randhir et al.  
77 2018), Ni-Zn-ferrite(Fresno et al. 2009), and Ni-Mg-ferrite(Takalkar et al. 2020).

78 Mn-ferrite ( $MnFe_2O_4$ ) was also tested for H<sub>2</sub> generation via WS reactions. A redox system  
79 comprised of Mn-ferrite/ZnO/H<sub>2</sub>O was examined for WS application at 1273 K(Inoue et al. 2004).  
80 70% of the theoretical H<sub>2</sub> production is reported by Mn-ferrite nanoparticles produced via ball  
81 milling(Padella et al. 2005). Solid-state synthesized Mn-ferrite showed five times lower H<sub>2</sub>  
82 production aptitude than the Mn-ferrite prepared using high energy ball milling(Alvani et al.  
83 2005). The rate of H<sub>2</sub> production via WS reaction was higher in the case of Mn-ferrite as compared

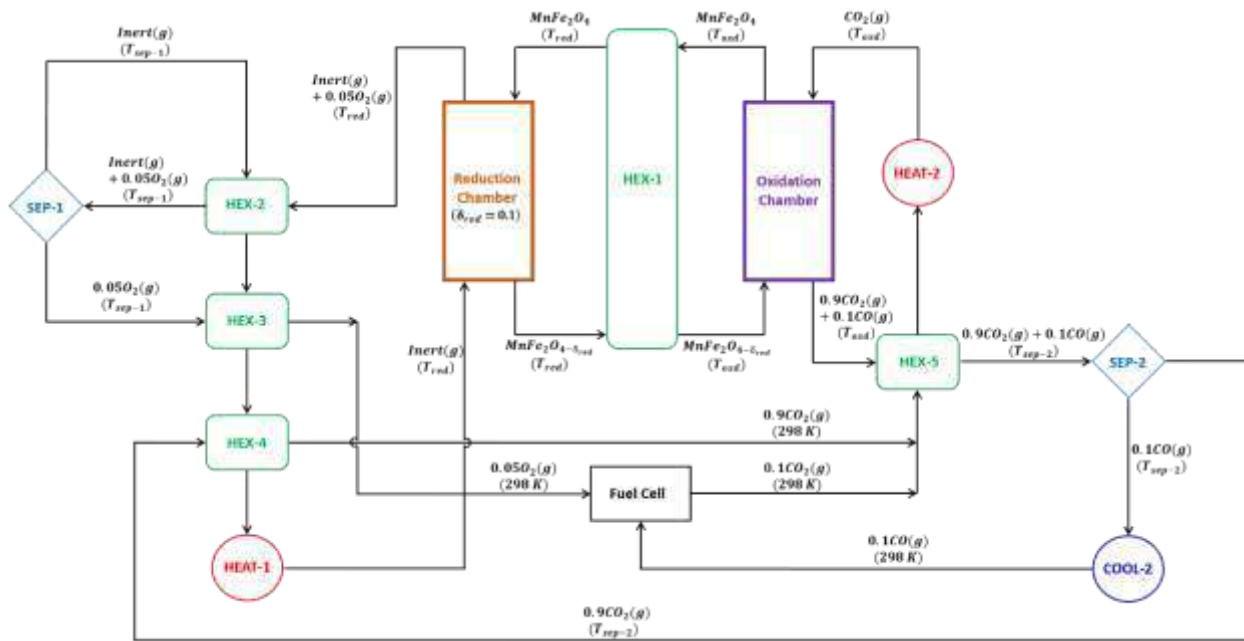
84 to  $ZnFe_2O_4$  and  $Fe_2O_3$  (Go et al. 2008). A powdered mixture comprised of Mn-ferrite and CaO  
85 produced 0.4 to 0.9 ml of  $H_2/g$  in three WS cycles performed at 1273 K (Tamura et al. 1998). A  
86 study also reported that the Mn-ferrite got segregated during the WS reaction (Ehrensberger et  
87 al. 1996). Sol-gel-derived Mn-ferrite nanoparticles were also tested for  $H_2$  production via  
88 thermochemical WS reaction (Bhosale et al. 2012).

89 All the studies mentioned above are experimental investigations of Mn-ferrite based WS  
90 cycle. Besides experimentally determined fuel production capacity, estimation of solar-to-fuel  
91 energy conversion efficiency ( $\eta_{solar-to-fuel}$ ) is also an essential step towards the judgment of  
92 a MO's suitability for solar thermochemical cycles. Recently,  $\eta_{solar-to-fuel}$  of Mn-ferrite based  
93 WS cycle has been reported (Bhosale 2019b). However, this study estimates  $\eta_{solar-to-fuel}$   
94 without considering the thermal energy requirements allied with the heating of inert  
95 sweeping gas and separation of gaseous components. Besides, the utilization of Mn-ferrite  
96 based redox reactions for CDS is not yet studied. Hence, in this investigation, a theoretical  
97 model for the  $MnFe_2O_4$  based CDS cycle is developed and a detailed thermodynamic efficiency  
98 analysis is carried out.  $\eta_{solar-to-fuel}$  is calculated by considering the energy penalties  
99 associated with the heating of inert sweep gas and separation of inert/ $O_2$  and  $CO_2/CO$  gas  
100 mixtures.

## 101 **2. Thermodynamic Model and Equations**

102 By considering the following assumptions, a thermodynamic model is developed for the  
103 determination of  $\eta_{solar-to-fuel}$  and other process parameters of  $MnFe_2O_4$  based CDS cycle.  
104 The developed thermodynamic model is presented in Fig. 1.

105



106

107

Fig. 1. Schematic of the process model of  $MnFe_2O_4$  based  $CO_2$  splitting cycle.

108

1) All processes operated at steady-state

109

2) Ideal gas behavior

110

3) Reduction, as well as oxidation chambers, are operated at isothermal conditions

111

4) Chemical equilibrium between the  $MnFe_2O_4$  and the gases

112

5) The efficiency of an Ideal  $CO_2/CO$  fuel cell equal to 100%

113

6) All reactions undergo complete conversion

114

7) Kinetic/potential energy and viscous losses are not considered

115

8) No side reactions

116

9) 20% of thermal energy losses from the reduction chamber

117

10) All the calculations are standardized to  $\dot{n}_{MnF} = 1 \text{ mol/s}$

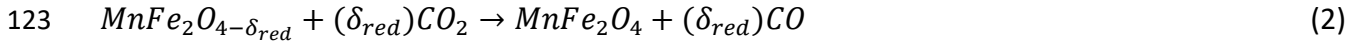
118

As shown in Fig. 1, separate reaction chambers are installed to reduce and re-oxidize the Mn-

119

ferrite, as per Eqs. (1) and (2). These two chambers are operated isothermally, i.e., the reduction

120 chamber at reduction temperature ( $T_{red}$ ) and the re-oxidation chamber at oxidation  
121 temperature ( $T_{oxd}$ ).



124 The equations listed above shows that the reduction and re-oxidation of  $MnFe_2O_4$  occurs in two  
125 separate steps. Step-1 deals with the release of  $O_2$  due to thermal reduction of  $MnFe_2O_4$ . On the  
126 other hand, re-oxidation of  $MnFe_2O_{4-\delta_{red}}$  is carried out in step-2, which results in the production  
127 of CO vi thermochemical CDS. All the calculations are performed by assuming  $\delta_{red} = 0.1$ .

128 The inert sweeping gas method is applied to maintain the partial pressure of  $O_2$  in the  
129 reduction chamber. The entrance of the inert sweep gas in the reduction chamber is located at  
130 the state  $red_1$ . Likewise, state  $red_2$  indicate the exit of the inert sweep gas from the reduction  
131 chamber.  $MnFe_2O_4$  is shuttled in the reduction chamber from state  $red_3$  to  $red_4$ . Estimation of  
132 the heat energy needed for the thermal reduction of  $MnFe_2O_4$  is carried out by using the  
133 following equation.

$$134 \quad \dot{Q}_{MnF-red} = \dot{n}_{MnF} \Delta H |_{MnFe_2O_4 \rightarrow MnFe_2O_{4-\delta_{red}} + \frac{\delta_{red}}{2} O_2} \quad (3)$$

135 By using Eq.(4), the thermal energy needed for the heating of  $MnFe_2O_4$  from  $T_{oxd}$  to  $T_{red}$  is  
136 calculated.

$$137 \quad \dot{Q}_{MnF-sens} = \dot{n}_{MnF} \Delta H |_{MnFe_2O_4 @ T_{oxd} \rightarrow MnFe_2O_4 @ T_{red}} \quad (4)$$

138 Thermal reduction of  $MnFe_2O_4$  results in the release of  $O_2$  from the ferrite crystal lattice. The  
139 released  $O_2$  is further conveyed away from the reduction chamber with the help of inert sweep  
140 gas. After exiting the reduction chamber, the gas mixture containing inert sweep gas and  $O_2$  is

141 cooled down from  $T_{red}$  to  $T_{sep-1}$  by using HEX-2 (gas-to-gas heat exchanger). After cooling, the  
 142 gas mixture is further transported to separator-1 to separate  $O_2$  from the inert sweep gas. The  
 143 separator-1 is operated with an assumed efficiency ( $\eta_{sep-1}$ ) equal to 15% and as per the process  
 144 described in published literature (Ehrhart et al. 2016). The heat energy required for the  
 145 separation of  $O_2$  from inert sweep gas is calculated as per the following set of equations:

$$146 \quad \dot{Q}_{sep-1} = \dot{n}_{MnF} \left[ \frac{T_{sep-1}}{\eta_{sep-1}} (\Delta S_{mix,red_2} - \Delta S_{mix,red_1}) \right] \quad (5)$$

$$147 \quad \Delta S_{mix,red_1} = -R \{ n_{inert} \ln(1 - y_{O_2,red_1}) + n_{O_2,red_1} \ln y_{O_2,red_1} \} \quad (6)$$

$$148 \quad \Delta S_{mix,red_2} = -R \{ n_{inert} \ln(1 - y_{O_2,red_2}) + n_{O_2,red_2} \ln y_{O_2,red_2} \} \quad (7)$$

149 HEX-3 (gas-to-gas heat exchanger) is placed in the model to reduce the temperature of  $O_2$   
 150 separated from the inert sweep gas from  $T_{sep-1}$  to  $T_0 = 298$  K. After cooling,  $O_2$  is transferred to  
 151 an ideal CO/ $O_2$  fuel cell. The inert sweep gas, separated from the  $O_2$ , is heated from  $T_{sep-1}$  to  
 152  $T_{red}$  by going through a series of three gas-to-gas heat exchangers, namely, HEX-1, HEX-2, and  
 153 HEX-3. If required, supplementary heat is also provided with the help of an auxiliary heater-1.  
 154 The energy required to heat the inert sweep gas is estimated as follows:

$$155 \quad \dot{Q}_{inert-heat} = \varepsilon_{gg} [\dot{Q}_{(inert+O_2)-cool} + \dot{Q}_{O_2-cool} + \dot{Q}_{CO_2-cool}] + \dot{Q}_{heater-1} \quad (8)$$

156 Where,

$$157 \quad \dot{Q}_{inert-heat} = \dot{n}_{inert} \Delta H |_{inert@T_{sep-1} \rightarrow inert@T_{red}} \quad (9)$$

$$158 \quad \dot{Q}_{(inert+O_2)-cool} = \dot{n}_{inert} \Delta H |_{inert@T_{red} \rightarrow inert@T_{sep-1}} + \dot{n}_{O_2} \Delta H |_{O_2@T_{red} \rightarrow O_2@T_{sep-1}} \quad (10)$$

$$159 \quad \dot{Q}_{O_2-cool} = \dot{n}_{O_2} \Delta H |_{O_2@T_{sep-1} \rightarrow O_2@T_0} \quad (11)$$

$$160 \quad \dot{Q}_{CO_2-cool} = \dot{n}_{CO_2} \Delta H|_{CO_2@T_{sep-2} \rightarrow CO_2@T_0} \quad (12)$$

161 To carry out the thermochemical CDC, CO<sub>2</sub> (in an excess amount, 10δ<sub>red</sub>) enters the oxidation  
 162 chamber at the state *oxd*<sub>3</sub>. After completion of the CDC reaction, a gas mixture comprised of  
 163 unreacted CO<sub>2</sub> and produced CO leaves the oxidation chamber at the state *oxd*<sub>4</sub>. Alternatively,  
 164 *MnFe<sub>2</sub>O<sub>4-δ<sub>red</sub></sub>* is shuttled from states *oxd*<sub>3</sub> to *oxd*<sub>4</sub> in a counter-current fashion relative to the  
 165 gases encountered. As the CDC reaction is carried out at *T*<sub>oxd</sub> = 1000 K, the temperature of  
 166 *MnFe<sub>2</sub>O<sub>4-δ<sub>red</sub></sub>* is decreased from *T*<sub>red</sub> to *T*<sub>oxd</sub> with the help of HEX-1 (solid-to-solid heat  
 167 exchanger). As the solid-to-solid heat recovery effectiveness (*ε*<sub>SS</sub>) is assumed to be zero, the heat  
 168 energy liberated during the cooling of *MnFe<sub>2</sub>O<sub>4-δ<sub>red</sub></sub>* is not reused for the heating of *MnFe<sub>2</sub>O<sub>4</sub>*.  
 169 The heat dissipated during CO production vis CDC is computed by using the following equation.

$$170 \quad \dot{Q}_{MnF-oxd} = -\dot{n}_{MnF} \Delta H|_{MnFe_2O_{4-\delta_{red}} + (10\delta_{red})CO_2 \rightarrow MnFe_2O_4 + (10\delta_{red} - \delta_{red})CO_2 + (\delta_{red})CO} \quad (13)$$

171  $\dot{Q}_{MnF-oxd}$  is assumed to be rejected to the ambient.

172 HEX-5 (gas-to-gas heat exchanger) and an auxiliary heater-2 are installed in the model to pre-  
 173 heat CO<sub>2</sub> from *T*<sub>0</sub> to *T*<sub>oxd</sub>. Eq. (14) is used to calculate the heating energy in the case of the CO<sub>2</sub>.

$$174 \quad \dot{Q}_{CO_2-heat} = \epsilon_{gg} [\dot{Q}_{(CO_2+CO)-cool}] + \dot{Q}_{heater-2} \quad (14)$$

175 Where,

$$176 \quad \dot{Q}_{CO_2-heat} = \dot{n}_{CO_2} \Delta H|_{CO_2@T_0 \rightarrow CO_2@T_{oxd}} \quad (15)$$

$$177 \quad \dot{Q}_{(CO_2+CO)-cool} = \dot{n}_{CO_2} \Delta H|_{CO_2@T_{oxd} \rightarrow CO_2@T_{sep-2}} + \dot{n}_{CO} \Delta H|_{CO@T_{oxd} \rightarrow CO@T_{sep-2}} \quad (16)$$

178 The reuse of CO<sub>2</sub> is possible only if it is separated from CO, for which a separator-2 is included.  
 179 Separator-2 is operated at  $T_{sep-2} = 400$  K and efficiency ( $\eta_{sep-2}$ ) equal to 15% (Carrillo and  
 180 Scheffe 2019). As the CO<sub>2</sub>/CO separation is carried out at 400 K, the CO<sub>2</sub>/CO gas mixture  
 181 temperature is reduced from  $T_{oxd}$  to  $T_{sep-2}$  by passing through HEX-5. Following three equations  
 182 are used for determining  $\dot{Q}_{sep-2}$  (heat energy needed for the separation).

$$183 \quad \dot{Q}_{sep-2} = \dot{n}_{MnF} \left[ \frac{T_{sep-2}}{\eta_{sep-2}} (\Delta S_{mix,oxd_4} - \Delta S_{mix,oxd_3}) \right] \quad (17)$$

$$184 \quad \Delta S_{mix,oxd_3} = -R \{ n_{CO_2} \ln(1 - y_{CO,oxd_3}) + n_{CO,oxd_3} \ln y_{CO,oxd_3} \} \quad (18)$$

$$185 \quad \Delta S_{mix,oxd_4} = -R \{ n_{CO_2} \ln(1 - y_{CO,oxd_4}) + n_{CO,oxd_4} \ln y_{CO,oxd_4} \} \quad (19)$$

186 CO separated from the CO<sub>2</sub>/CO gas mixture is further cooled down to  $T_0$  with the help of an  
 187 auxiliary cooler-1 (heat rejected to the ambient). CO at 298 K is then transported to the fuel cell,  
 188 which is installed in the model to complete the thermochemical  $MnFe_2O_4-\delta_{red}$  based CDC cycle.  
 189 The fuel cell's outlet stream, which is CO<sub>2</sub> at 298 K, is first mixed with the unreacted CO<sub>2</sub>  
 190 (separated from the CO) and then transferred to the oxidation chamber via passing through HEX-  
 191 5 and heater-2.

192 The total amount of heat energy essential for the operation of  $MnFe_2O_4$  based CDS cycle is  
 193 computed by using Eq.(20)

$$194 \quad \dot{Q}_{TC} = \dot{Q}_{MnF-red} + \dot{Q}_{MnF-sens} + \dot{Q}_{heater-1} + \dot{Q}_{heater-2} + \dot{Q}_{sep-1} + \dot{Q}_{sep-2} + \dot{Q}_{surf} \quad (20)$$

195 Where,

$$196 \quad \dot{Q}_{surf} = 0.2 \times \dot{Q}_{MnF-red} \quad (21)$$

197 For the estimation of solar-to-fuel energy conversion efficiency ( $\eta_{solar-to-fuel}$ ) it is important  
 198 first to calculate the solar energy required to drive the cycle ( $\dot{Q}_{solar}$ ). Hence,  $\dot{Q}_{solar}$  is  
 199 determined by using the following set of equations.

$$200 \quad \dot{Q}_{solar} = \frac{\dot{Q}_{TC}}{\eta_{absorption}} \quad (22)$$

201 Here,

$$202 \quad \eta_{absorption} = 1 - \left( \frac{\sigma T_{red}^4}{IC} \right) \quad (23)$$

203 For the estimation of  $\eta_{absorption}$ ,  $\sigma$ ,  $I$ , and  $C$  are taken as  $5.6705 \times 10^{-8} \text{ W/m}^2 \cdot \text{K}^4$ ,  $1000 \text{ W/m}^2$ ,  
 204 and 3000 suns, respectively.

205 Re-radiation losses from the model are also calculated by using Eq.(24)

$$206 \quad \dot{Q}_{re-rad} = \eta_{absorption} \times \dot{Q}_{solar} \quad (24)$$

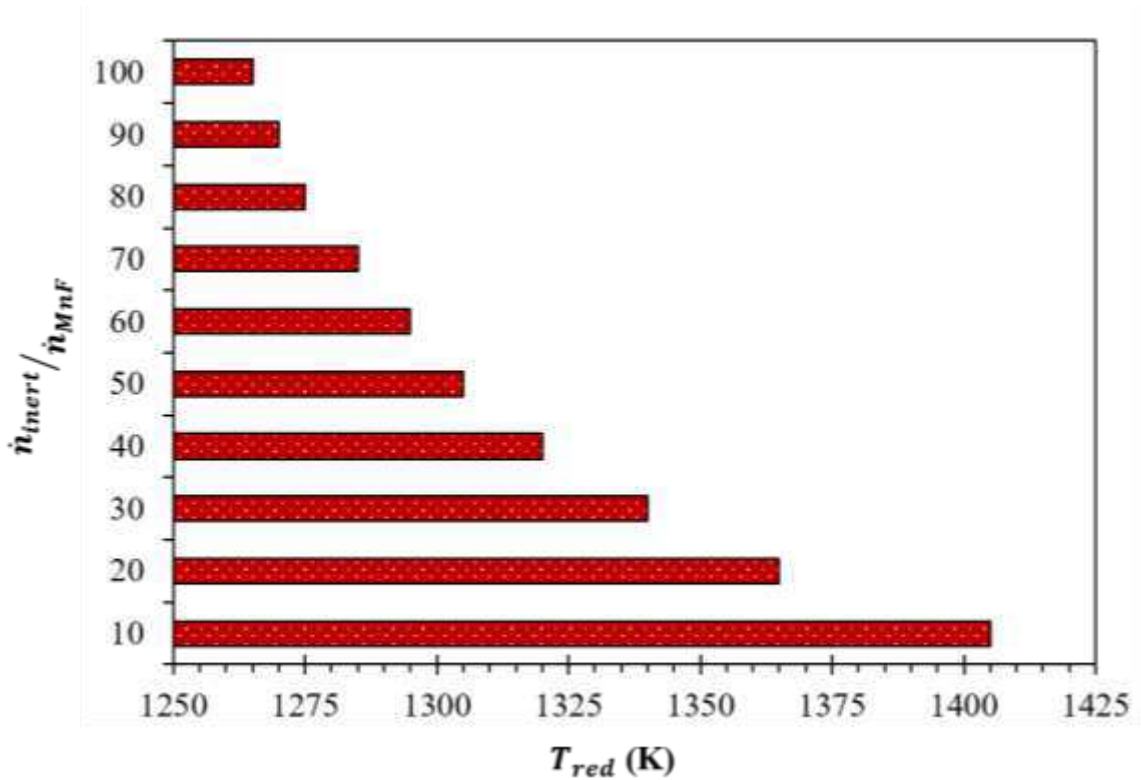
207 Finally,  $\eta_{solar-to-fuel}$  is estimated as follows:

$$208 \quad \eta_{solar-to-fuel} = \frac{\dot{n}_{CO} \times HHV_{CO}}{\dot{Q}_{solar}} \quad (25)$$

### 209 **3. Results and Discussion**

210 Reduction temperature ( $T_{red}$ ) required for attaining  $\delta_{red} = 0.1$  is estimated as a function  
 211 of the ratio of the molar flow rates of inert sweep gas ( $\dot{n}_{inert}$ ) and  $MnFe_2O_4$  ( $\dot{n}_{MnF}$ ), i.e.,  
 212  $\dot{n}_{inert}/\dot{n}_{MnF}$ . As per the data presented in Fig. 2, the highest  $T_{red}$  equal to 1405 K is recorded for  
 213  $\dot{n}_{inert}/\dot{n}_{MnF}$  equal to 10. A further rise in  $\dot{n}_{inert}/\dot{n}_{MnF}$  from 10 to 100 reduces  $T_{red}$  from 1405 K

214 to 1265 K. Interestingly, the decrease in  $T_{red}$  is higher (100 K) when  $\dot{n}_{inert}/\dot{n}_{MnF}$  upturns from  
 215 10 to 50 as compared to a rise in  $\dot{n}_{inert}/\dot{n}_{MnF}$  from 50 to 100 ( $T_{red}$  reduces by 40 K). These  
 216 observations confirm that the effect of  $\dot{n}_{inert}/\dot{n}_{MnF}$  on  $T_{red}$  is less weighty during the increment  
 217 in  $\dot{n}_{inert}/\dot{n}_{MnF}$  from 50 to 100.



218  
 219 Fig. 2. Effect of  $\dot{n}_{inert}/\dot{n}_{MnF}$  on the temperature required for the reduction ( $T_{red}$ ) of  $MnFe_2O_4$

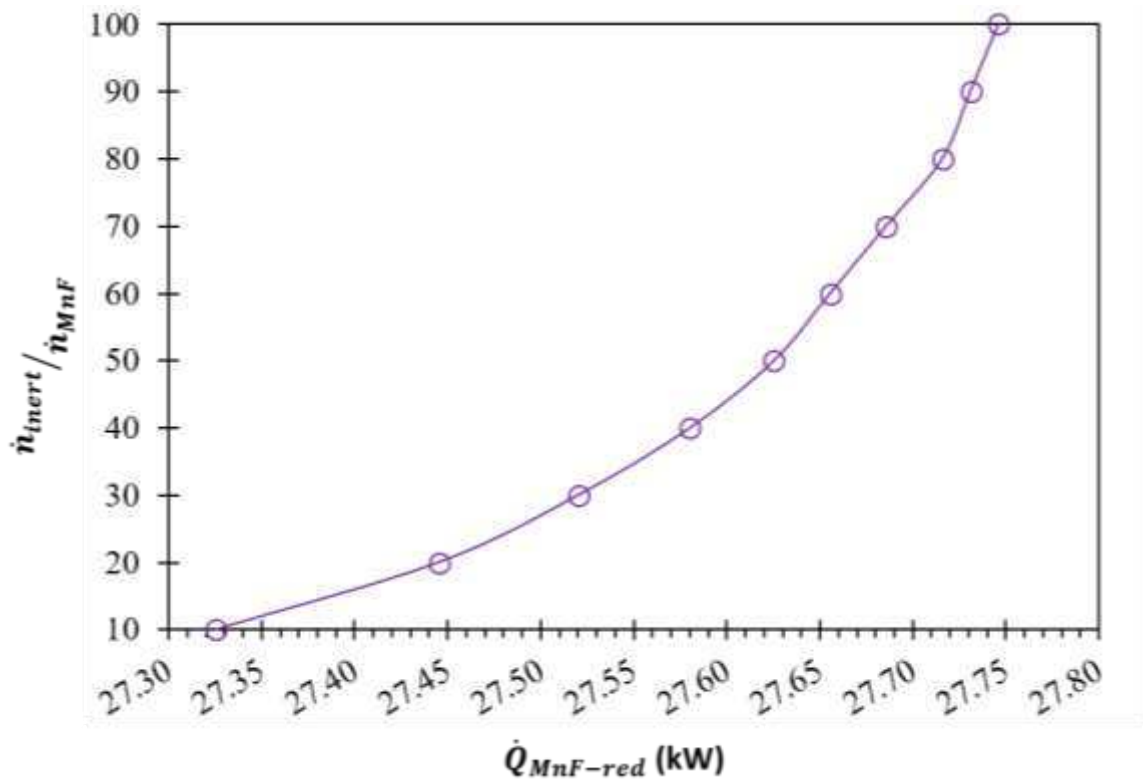
220  $(\delta_{red} = 0.1).$

221

222

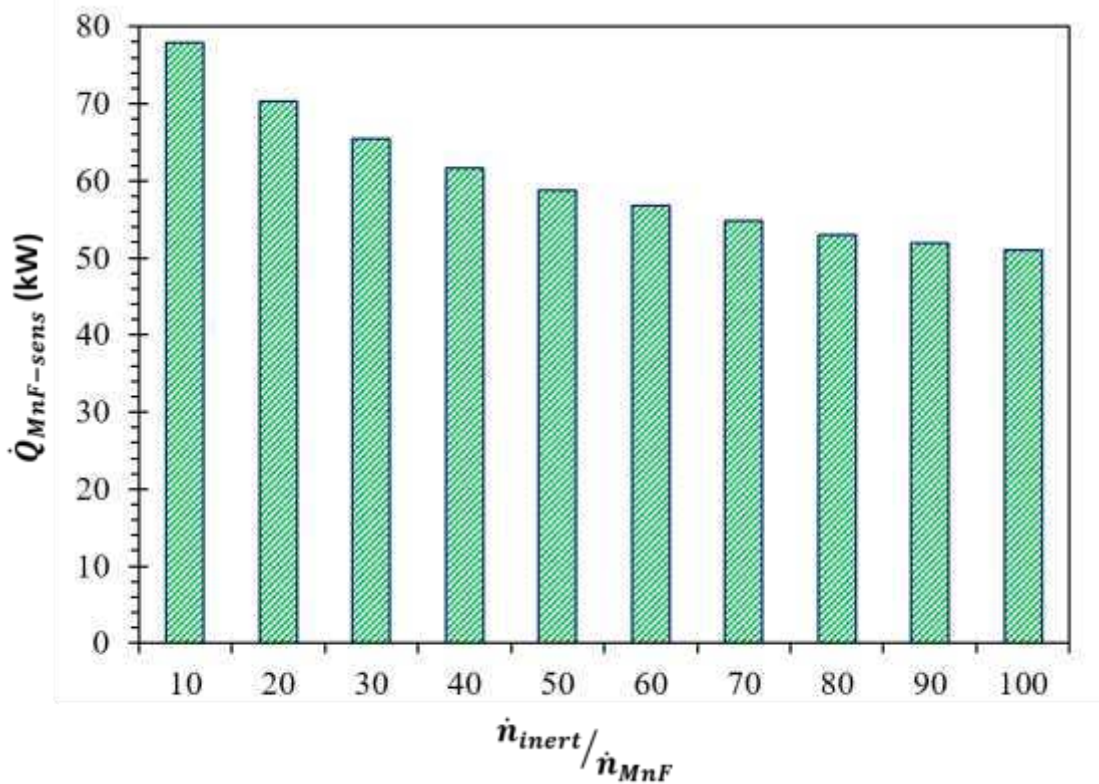
223

224 The effect of  $\dot{n}_{inert}/\dot{n}_{MnF}$  on the energy required for the reduction of  $MnFe_2O_4$  into  
 225  $MnFe_2O_{4-\delta_{red}}$  ( $\delta_{red} = 0.1$ ) is explored, and the obtained results are presented in Fig. 3. As the  
 226 pre-heating of both inert sweep gas and  $MnFe_2O_4$  are carried out separately (not in the  
 227 reduction chamber), the heat energy needed for both pre-heating operations are not included in  
 228 the computation of  $\dot{Q}_{MnF-red}$ . Presented results show that the rise in  $\dot{n}_{inert}/\dot{n}_{MnF}$  results in a  
 229 very minute change in  $\dot{Q}_{MnF-red}$ . As  $\dot{n}_{inert}/\dot{n}_{MnF}$  increases from 10 to 100, although  $T_{red}$   
 230 reduces by 140 K,  $\dot{Q}_{MnF-red}$  upsurges only by a factor of 1.02.



231  
 232 Fig. 3. Effect of  $\dot{n}_{inert}/\dot{n}_{MnF}$  on the thermal energy required ( $\dot{Q}_{MnF-red}$ ) for the reduction of  
 233  $MnFe_2O_4$  ( $\delta_{red} = 0.1$ ).

234 Eq.(4) is applied for the calculation of  $\dot{Q}_{MnF-sens}$ . As mentioned in section 2, heat energy  
 235 dissipated during the cooling of  $MnFe_2O_4-\delta_{red}$  is not recuperated for the pre-heating of  
 236  $MnFe_2O_4$ . Variations recorded in  $\dot{Q}_{MnF-sens}$  due the rise in  $\dot{n}_{inert}/\dot{n}_{MnF}$  are presented in Fig. 4.  
 237 The reported trends show that the change in  $T_{red}$  has a considerable effect on  $\dot{Q}_{MnF-sens}$ . As per  
 238 the results,  $\dot{Q}_{MnF-sens}$  reduces below 77.9 kW by 16.0%, 24.6%, 29.6%, and 33.3% as the  $T_{red}$   
 239 decreases below 65 K, 100 K, 120 K, and 135 K due to the rise in  $\dot{n}_{inert}/\dot{n}_{MnF}$  from 10 to 30, 50,  
 240 70, and 90, respectively. Overall increase in  $\dot{n}_{inert}/\dot{n}_{ZnF}$  from 10 to 100 is responsible for the  
 241 reduction in  $\dot{Q}_{MnF-sens}$  from 77.9 kW to 51.0 kW, respectively.

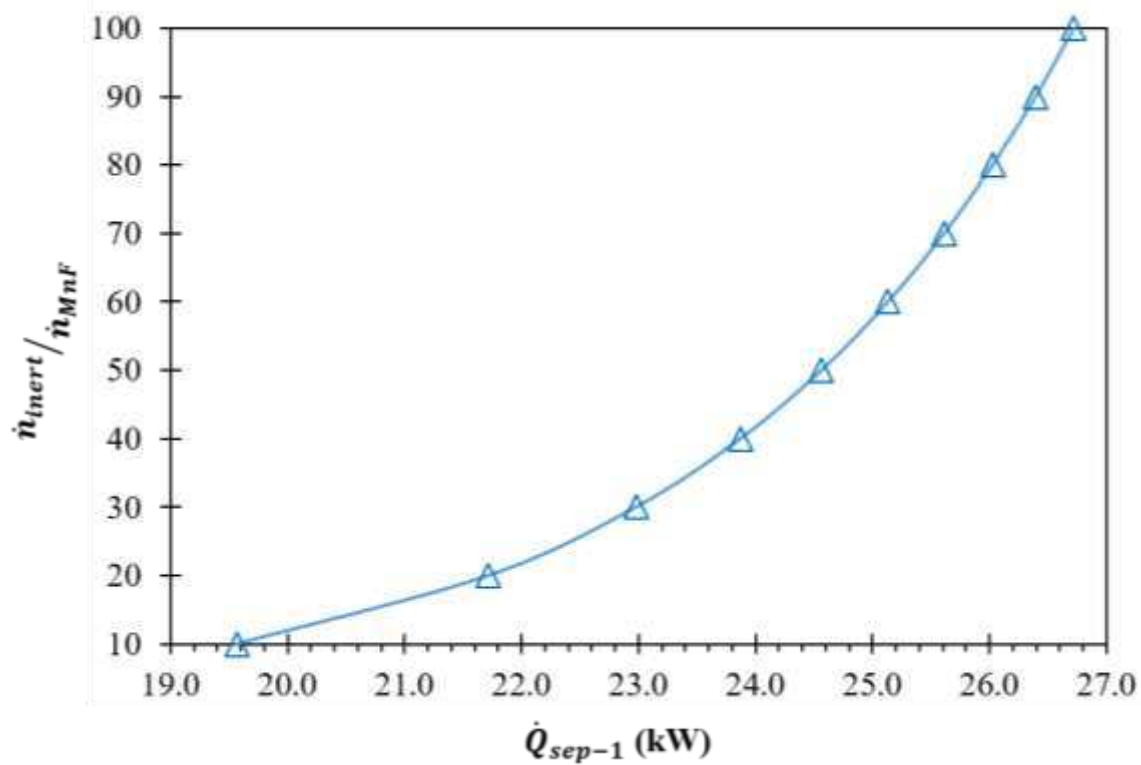


242  
 243 Fig. 4. Effect of  $\dot{n}_{inert}/\dot{n}_{MnF}$  on the thermal energy required ( $\dot{Q}_{MnF-sens}$ ) for the heating of  
 244  $MnFe_2O_4$  from oxidation temperature ( $T_{oxd}$ ) up to reduction temperature ( $T_{red}$ ).

245 As per the model presented in Fig. 1, after completion of the reduction step,  $MnFe_2O_{4-\delta_{red}}$   
246 is transported to the oxidation chamber. In this chamber, the re-oxidation of  $MnFe_2O_{4-\delta_{red}}$  is  
247 conducted at steady  $T_{oxd} = 1000$  K. As the molar compositions and reaction temperature stay  
248 unchanged,  $\dot{Q}_{MnF-oxd}$  remains stable at 0.3 kW. This heat energy is not utilized for any purpose  
249 and is rejected to the ambient.

250  $O_2$  released during the reduction of  $MnFe_2O_4$  get mixed with the inert sweeping gas and  
251 moves out of the reduction chamber. For the reuse of inert sweeping gas, the  $O_2$  has to be  
252 separated for this gas mixture. As this gas mixture has a temperature higher than 1000 K, ion  
253 transport membrane technology (operating temperature range: 1050 to 1200 K) is used for the  
254 separation (Anderson et al. 2016). The operating temperature of the separator-1 is assumed to  
255 be 1123 K. It is essential first to reduce the temperature of the gas mixture containing inert sweep  
256 gas and  $O_2$  from  $T_{red}$  to  $T_{sep-1}$ . This is achieved by passing this gas mixture through HEX-2.

257 After attaining the separation temperature (1123 K), the gas mixture comprised of inert  
258 sweep gas and  $O_2$  enters separator-1. Here, 99.9% of  $O_2$  is separated from the inert sweeping  
259 gas. Eqs. (5) to (7) are applied for the determination of the heat energy required for the operation  
260 of separator-1 ( $\dot{Q}_{sep-1}$ ). All the calculations associated with the separator-1 are done based on  
261 the second law of thermodynamics ( $\Delta Q = T\Delta S$ ). Moreover, by estimating the entropy of mixing  
262 for each stream. As  $\dot{n}_{inert}/\dot{n}_{MnF}$  upsurges from 10 to 100,  $\dot{Q}_{sep-1}$  differs due to the variation in  
263 the mole fraction of  $O_2$  at the states  $red_1$  and  $red_2$ . As shown in Fig. 5, the rise in  $\dot{n}_{inert}/\dot{n}_{MnF}$   
264 from 10 to 30, 50, 70, and 90 results in an upturn in  $\dot{Q}_{sep-1}$  above 19.6 kW by 3.4 kW, 5.0 kW,  
265 6.0 kW, and 6.8 kW, respectively.



266

267 Fig. 5. Effect of  $\dot{n}_{inert} / \dot{n}_{MnF}$  on the thermal energy required for the operation of separator-1  
 268  $(\dot{Q}_{sep-1})$ .

269 The fuel cell is fed with the O<sub>2</sub>, which is first separated from the inert sweep gas and then  
 270 cooled to 298 K by passing through HEX-3. Alternatively, by going through HEX-2, HEX-3, HEX-4,  
 271 and heater-1, the inert sweep gas is pre-heated from  $T_{sep-1}$  to  $T_{red}$ . Table 1 reports the  
 272 influence of  $\dot{n}_{inert} / \dot{n}_{MnF}$  on  $\dot{Q}_{inert-heat}$ . Due to the increase in the  $\dot{n}_{inert} / \dot{n}_{MnF}$ , as per the  
 273 expectations,  $\dot{Q}_{inert-heat}$  surges substantially. For instance, as  $\dot{n}_{inert} / \dot{n}_{ZnF}$  rises from 10 to 50  
 274 and then to 100,  $\dot{Q}_{inert-heat}$  increase from 95.8 kW to 307.4 kW and 478.4 kW, respectively.

275

276

277 Table 1. Effect of  $\dot{n}_{inert}/\dot{n}_{MnF}$  on thermal energy required after each gas-to-gas heat  
 278 exchanger ( $\varepsilon_{gg} = 0.7$ ) for the pre-heating of inert sweep gas ( $\dot{Q}_{inert-heat}$ ).

$\dot{n}_{inert}/\dot{n}_{MnF}$	$T_{red}$ (K)	$\dot{Q}_{inert-heat}$ (kW)	$\dot{Q}_{inert-heat}$ Required		
			After HEX-2 (kW)	After HEX-3 (kW)	After HEX-4 (kW)
10	1405	95.8	28.4	27.5	24.9
20	1365	164.1	48.9	48.0	45.5
30	1340	220.4	65.8	64.9	62.4
40	1320	266.4	79.7	78.7	76.2
50	1305	307.4	92.0	91.0	88.5
60	1295	348.4	104.3	103.3	100.8
70	1285	382.6	114.6	113.6	111.1
80	1275	409.9	122.8	121.8	119.3
90	1270	445.9	133.6	132.6	130.1
100	1265	478.4	143.3	142.4	139.9

279  
 280 In HEX-2, heat energy released by inert/O<sub>2</sub> gas mixture during cooling from  $T_{red}$  to  $T_{sep-1}$   
 281 is utilized to pre-heat the inert sweep gas ( $\varepsilon_{gg} = 0.7$ ).  $\dot{Q}_{inert-heat}$  considerably decreased when  
 282 the inert sweep gas passes through the HEX-2. As an example,  $\dot{Q}_{inert-heat}$  drops from 95.8 kW,  
 283 307.4 kW, and 478.4 kW to 28.4 kW, 92.0 kW, and 143.3 kW at  $\dot{n}_{inert}/\dot{n}_{MnF}$  equal to 10, 50,  
 284 and 100, respectively.

285 After HEX-2, the inert sweep gas is then passed through HEX-3 ( $\varepsilon_{gg} = 0.7$ ) in which the  
286 cooling stream is O<sub>2</sub>, which came out of separator-2. In this gas-to-gas heat exchanger,  
287  $\dot{Q}_{inert-heat}$  decreases only by 0.9 kW for all  $\dot{n}_{inert}/\dot{n}_{MnF}$ . The reason for this lower drop in  
288  $\dot{Q}_{inert-heat}$  is the lower molar flow rate of O<sub>2</sub>.

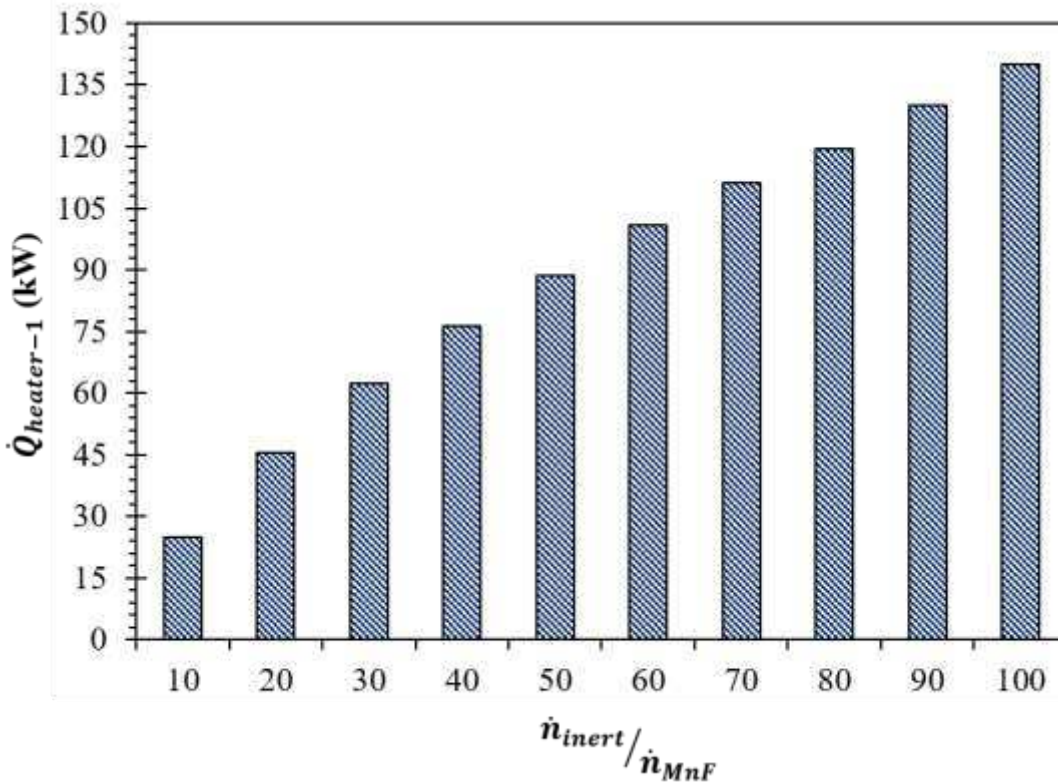
289 In HEX-4 ( $\varepsilon_{gg} = 0.7$ ), heat energy dissipated during the cooling of unreacted CO<sub>2</sub> is utilized to  
290 heat inert sweep gas. As the CO<sub>2</sub> molar flow rate is much higher than O<sub>2</sub>, as compared to HEX-3,  
291 the employment of HEX-4 is responsible for a more significant reduction in  $\dot{Q}_{inert-heat}$ . For all  
292 values of  $\dot{n}_{inert}/\dot{n}_{MnF}$ ,  $\dot{Q}_{inert-heat}$  decreases by 2.5 kW.

293 As shown in Table 1, even though a series of three gas-to-gas heat exchangers are installed,  
294 supplementary energy is still needed to heat inert sweep gas. Heater-1 provides the extra heat  
295 energy required. Due to the variation in  $\dot{n}_{inert}/\dot{n}_{MnF}$ ,  $\dot{Q}_{heater-1}$  also differs (Fig. 6). For example,  
296 as  $\dot{n}_{inert}/\dot{n}_{MnF}$  increases from 10 to 30, 50, 70, and 90,  $\dot{Q}_{heater-1}$  rises from 24.9 kW to 62.4 kW,  
297 88.5 kW, 111.1 kW, and 130.1 kW, respectively.

298 The laboratory-scale thermochemical CDS experiments are carried out by using an excess  
299 amount of CO<sub>2</sub>. Hence, in this thermodynamic study, the CO<sub>2</sub> molar flow rate equal to 10 times  
300  $\delta_{red}$  is used. After the completion of CDS, due to the excess supply of CO<sub>2</sub>, the oxidation  
301 chamber's exit gas composition contains unreacted CO<sub>2</sub> and CO produced. Unreacted CO<sub>2</sub> can be  
302 reutilized for the re-oxidation of  $MnFe_2O_{4-\delta_{red}}$  (as shown in Fig. 1). To do this, the separation of  
303 CO<sub>2</sub> from CO is necessary.

304

305



306

307 Fig. 6. Effect of  $\dot{n}_{inert}/\dot{n}_{MnF}$  on the thermal energy provided by heater-1 ( $\dot{Q}_{heater-1}$ ) for the  
 308 pre-heating of inert sweep gas.

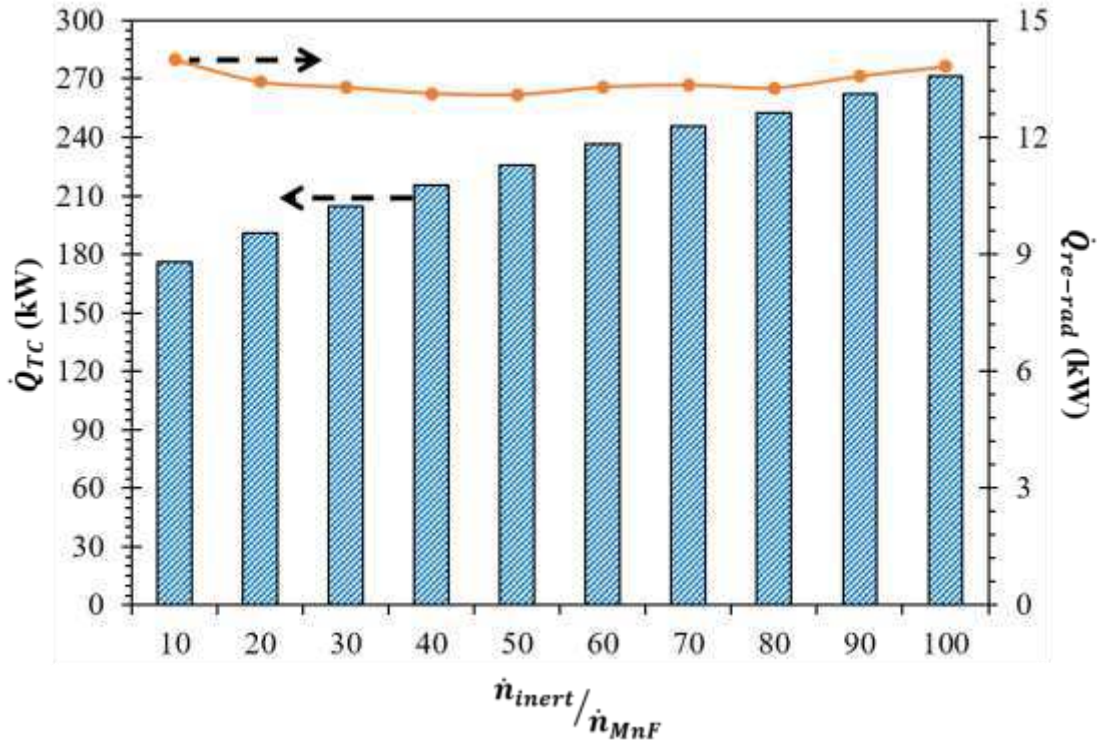
309 Separator-2 is installed in the process to separate CO<sub>2</sub> and CO gas mixture. It is operated at  
 310  $T_{sep-2} = 400$  K and hence the CO<sub>2</sub>/CO gas mixture, which exited the oxidation chamber at  $T_{oxd} =$   
 311 1000 K, is cooled by using HEX-5. After the reduction in the temperature, the CO<sub>2</sub>/CO gas mixture  
 312 enters the separator-2 ( $\eta_{sep-2} = 15\%$ ). Similar to separator-1, 99.9% of CO is separated from the  
 313 CO<sub>2</sub> stream. The heat energy required to achieve this separation ( $\dot{Q}_{sep-2}$ ) is calculated by solving  
 314 Eqs. (17) to (19). The thermodynamic computations indicate that the mole fraction of CO remains  
 315 stable at states  $oxd_3$  and  $oxd_4$ , even though  $\dot{n}_{inert}/\dot{n}_{MnF}$  increases from 10 to 100. Due to this,  
 316 a stable value of 7.2 kW is recorded for  $\dot{Q}_{sep-2}$  (for all values of  $\dot{n}_{inert}/\dot{n}_{MnF}$ ).

317 A supplementary cooler-1 is installed in the model to reduce the temperature of CO  
318 (separated from the CO<sub>2</sub>/CO gas mixture) from  $T_{sep-2}$  to  $T_0$ . The heat energy dissipated during  
319 this cooling is assumed to be rejected to the ambient. As an essential step to close the cycle, CO  
320 is then transported to the fuel cell and reacts with the O<sub>2</sub>, producing CO<sub>2</sub>.

321 CO<sub>2</sub> generated via the fuel cell reaction is then mixed with the unreacted CO<sub>2</sub>. Before entering  
322 into the oxidation chamber, the temperature of the CO<sub>2</sub> needs to be increased from 298 K up to  
323  $T_{oxd} = 1000$  K. This is achieved by using HEX-5 and a supplementary heater-2. It is important to  
324 note that, even though  $\dot{n}_{inert}/\dot{n}_{MnF}$  increases from 10 to 100, the molar flow rate of CO<sub>2</sub> entering  
325 and exiting the HEX-5 and heater-2 is steady. Hence, after passing through HEX-5, the additional  
326 heat needed for the heating, i.e.,  $\dot{Q}_{heater-2}$  remains unchanged at 13.6 kW

327 As mentioned in section 2 and as per the previously published work (Lu et al. 2019), it is  
328 assumed that 20% of the heat energy associated with the reduction chamber is lost to the  
329 ambient due to the issues associated with the thermal insulation. By considering these surface  
330 heat losses and other necessary heat energy requirements,  $\dot{Q}_{TC}$  needed to drive the cycle is  
331 estimated as per Eq.(20). Fig. 7 shows the effect of change in  $\dot{n}_{inert}/\dot{n}_{MnF}$  on  $\dot{Q}_{TC}$ . It is visible  
332 from the plot that rise in  $\dot{n}_{inert}/\dot{n}_{MnF}$  yields into an increase in  $\dot{Q}_{TC}$ . For example,  $\dot{Q}_{TC}$  mounts  
333 above 176.0 kW by 28.6 kW, 49.7 kW, 69.5 kW, and 86.5 kW due to the increment in  $\dot{n}_{inert}/\dot{n}_{MnF}$   
334 from 10 to 30, 50, 70, and 90, respectively. The reason for the enhancement in  $\dot{Q}_{TC}$  is the upsurge  
335 in  $\dot{Q}_{heater-1}$  and  $\dot{Q}_{sep-1}$  as a function of rise in  $\dot{n}_{inert}/\dot{n}_{MnF}$ .

336



337

338 Fig. 7. Effect of  $\dot{n}_{inert}/\dot{n}_{MnF}$  on the thermal energy required to operate  $MnFe_2O_4$  based  $CO_2$   
 339 splitting cycle ( $\dot{Q}_{TC}$ ) and re-radiation losses ( $\dot{Q}_{re-rad}$ ).

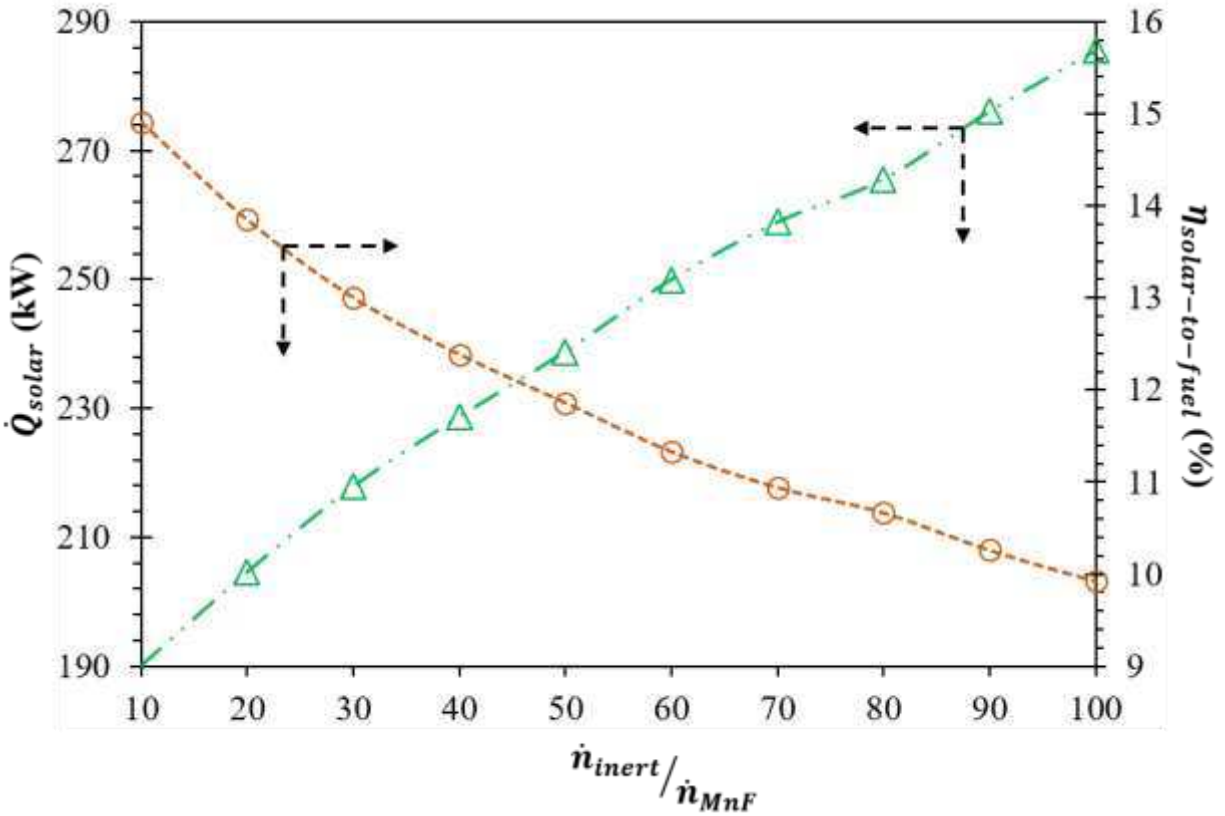
340 After estimating  $\dot{Q}_{TC}$ ,  $\dot{Q}_{solar}$  and  $\dot{Q}_{re-rad}$  are calculated by employing Eqs. (22) and (24). Figs.  
 341 7 and 8 present the divergences allied with both  $\dot{Q}_{re-rad}$  and  $\dot{Q}_{solar}$ . Both  $\dot{Q}_{solar}$  and  $\dot{Q}_{re-rad}$   
 342 depends upon  $\eta_{absorption}$ , which in turn rely on  $T_{red}$ .  $\eta_{absorption}$  of this cycle increases from  
 343 92.6% to 95.2% due to the drop in  $T_{red}$  from 1405 K to 1265 K. This rise in  $\eta_{absorption}$  indicates  
 344 that a higher percentage of solar energy is absorbed and hence  $\dot{Q}_{re-rad}$  losses are lower (Fig. 7).  
 345 On the other hand, as  $\eta_{absorption}$  is less than 100%,  $\dot{Q}_{solar}$  is recorded to be higher than  $\dot{Q}_{TC}$  for  
 346 all  $\dot{n}_{inert}/\dot{n}_{MnF}$  values. For example,  $\dot{Q}_{solar}$  is recorded to be higher than  $\dot{Q}_{TC}$  by 14.0 kW, 13.3  
 347 kW, 13.1 kW, 13.3 kW, and 13.6 kW at  $\dot{n}_{inert}/\dot{n}_{MnF}$  equal to 10, 30, 50, 70, and 90, respectively.

348 Fig. 8 shows the effect of  $\dot{n}_{inert}/\dot{n}_{MnF}$  on  $\eta_{solar-to-fuel}$ . For the estimation of  
 349  $\eta_{solar-to-fuel}$ , Eq.(25) is used. In this equation, the numerator is steady as  $\dot{n}_{CO}$  and  $HHV_{CO}$   
 350 are stable at 0.1 and 283.24 kW, respectively. Enhancement in  $\dot{n}_{inert}/\dot{n}_{MnF}$  is responsible for a  
 351 rise in  $\dot{Q}_{solar}$  which in turn reduces  $\eta_{solar-to-fuel}$ . For example, as  $\dot{n}_{inert}/\dot{n}_{MnF}$  increases from  
 352 10 to 30, 50, 70, and 90,  $\dot{Q}_{solar}$  also rises from 190.0 kW up to 217.8 kW, 238.8 kW, 258.9 kW,  
 353 and 276.1 kW, respectively. This increment in  $\dot{Q}_{solar}$  is responsible for the decrease in  
 354  $\eta_{solar-to-fuel}$  from 14.9% to 13.0%, 11.9%, 10.9%, and 10.3% when  $\dot{n}_{inert}/\dot{n}_{MnF}$  upsurges  
 355 from 10 to 30, 50, 70, and 90, respectively. The obtained results confirm that the maximum  
 356  $\eta_{solar-to-fuel}$  (14.9%) is attainable at  $\dot{n}_{inert}/\dot{n}_{MnF}$  equal to 10 ( $T_{red} = 1405$  K,  $T_{oxd} = 1000$  K,  
 357  $\epsilon_{gg} = 0.7$ , and  $\epsilon_{ss} = 0$ ).

358 The results reported until now confirm that the prime reason for the increment in  $\dot{Q}_{solar}$  and  
 359 reduction in  $\eta_{solar-to-fuel}$  is the rise in  $\dot{Q}_{MnF-sens}$ ,  $\dot{Q}_{heater-1}$ , and  $\dot{Q}_{CO_2-heat}$  as  $\dot{n}_{inert}/\dot{n}_{MnF}$   
 360 upturns from 10 to 100. All the calculations are conducted by assuming  $\epsilon_{ss}$  and  $\epsilon_{gg}$  constant at  
 361 0.0 and 0.7, respectively. It is a well-known fact that solids' heat recovery to solids is very  
 362 difficult and not often used. On the other hand, gas to gas heat recovery is commonly used  
 363 in the industry with gas-to-gas heat exchangers. To explore further, the effect of variation in  
 364  $\epsilon_{gg}$  (from 0.0 to 0.9) on  $\dot{Q}_{solar}$  and  $\eta_{solar-to-fuel}$  is investigated here. 100% gas-to-gas heat  
 365 recovery ( $\epsilon_{gg} = 1$ ) is not practical and hence not considered.

366

367



368

369 Fig. 8. Effect of  $\dot{n}_{inert}/\dot{n}_{MnF}$  on solar energy required to drive  $MnFe_2O_4$  based  $CO_2$  splitting  
 370 cycle ( $\dot{Q}_{solar}$ ) and solar-to-fuel energy conversion efficiency ( $\eta_{solar-to-fuel}$ ).

371 Results indicate that  $\dot{Q}_{MnF-red}$  and  $\dot{Q}_{MnF-sens}$  remains unaltered due to the variation in  $\epsilon_{gg}$ .

372 Conversely,  $\dot{Q}_{heater-1}$  and  $\dot{Q}_{heater-2}$  are recorded to be varied considerably when  $\epsilon_{gg}$  increases

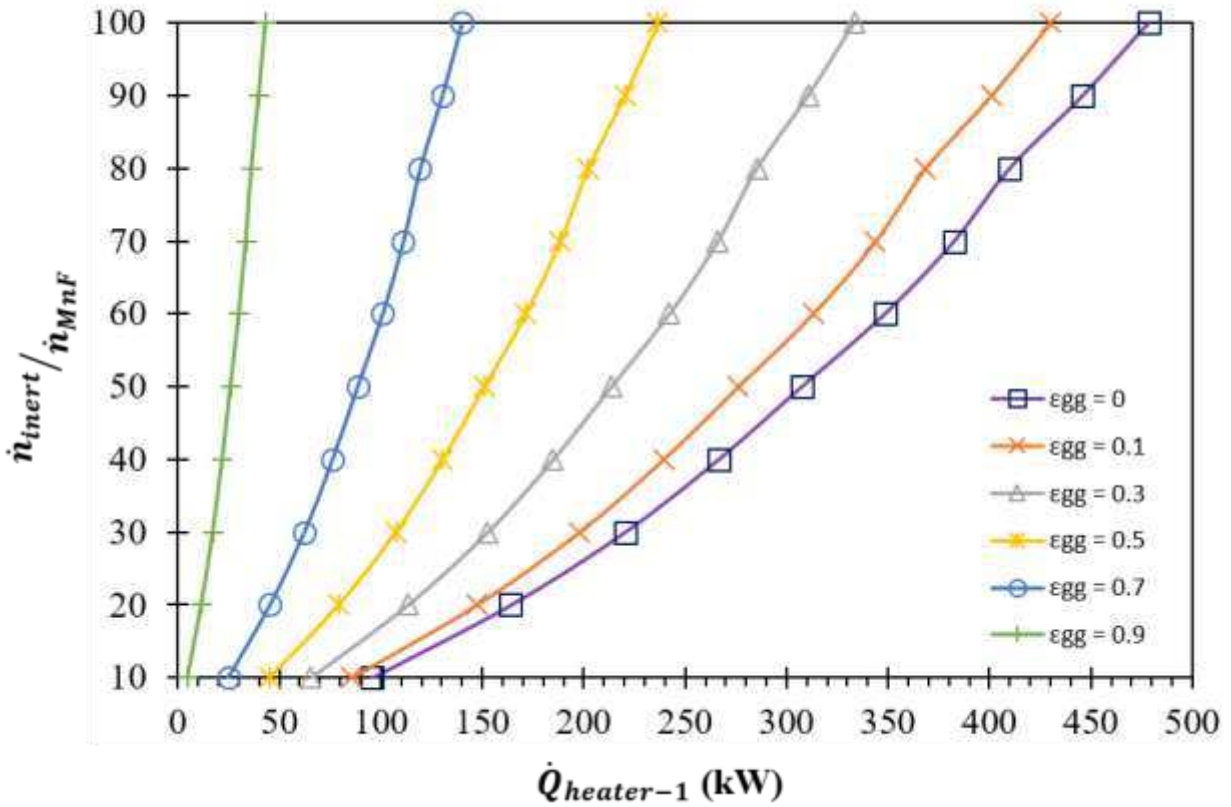
373 from 0.0 to 0.9. As per the trends reported in Fig. 9, at steady  $\dot{n}_{inert}/\dot{n}_{MnF}$ , a rise in  $\epsilon_{gg}$  yields

374 into a significant reduction in  $\dot{Q}_{heater-1}$ . For example, at  $\dot{n}_{inert}/\dot{n}_{MnF} = 10$ ,  $\dot{Q}_{heater-1}$  decreases

375 by 91.2 kW when  $\epsilon_{gg}$  surges from 0.0 to 0.9. Due to the similar upturn in  $\epsilon_{gg}$ ,  $\dot{Q}_{heater-1}$

376 diminishes by 435.5 kW at  $\dot{n}_{inert}/\dot{n}_{MnF}$  equal to 100.

377



378

379 Fig. 9. Effect of  $\dot{n}_{inert} / \dot{n}_{MnF}$  and gas-to-gas heat recovery effectiveness ( $\epsilon_{gg}$ ) on the thermal  
 380 energy provided by heater-1 ( $\dot{Q}_{heater-1}$ ) for the pre-heating of inert sweep gas.

381 The influence of  $\epsilon_{gg}$  on  $\dot{Q}_{heater-2}$  is reported in Table 2. It is already understood that the  
 382 rise in  $\dot{n}_{inert} / \dot{n}_{MnF}$  from 10 to 100 does not affect  $\dot{Q}_{heater-2}$ . Opposite to this, increment in  $\epsilon_{gg}$   
 383 decreases  $\dot{Q}_{heater-2}$ . The values reported in Table 2 shows that  $\dot{Q}_{heater-2}$  declines below 33.4  
 384 kW by 8.4%, 25.4%, 42.5%, 59.3%, and 76.3% due to the rise in  $\epsilon_{gg}$  from 0.1 to 0.3, 0.5, 0.7, and  
 385 0.9, respectively (for all  $\dot{n}_{inert} / \dot{n}_{MnF}$ ).

386

387

388 Table 2. Effect of gas-to-gas heat recovery effectiveness ( $\varepsilon_{gg}$ ) on the thermal energy provided

389 by heater-2 ( $\dot{Q}_{heater-2}$ ) for the pre-heating of CO<sub>2</sub> (for all  $\dot{n}_{inert}/\dot{n}_{MnF}$ ).

$\varepsilon_{gg}$	$\dot{Q}_{heater-2}$ (kW)
0.0	33.4
0.1	30.6
0.3	24.9
0.5	19.2
0.7	13.6
0.9	7.9

390

391 Fig. 10 shows that the rise in  $\varepsilon_{gg}$  reduces  $\dot{Q}_{TC}$  for all  $\dot{n}_{inert}/\dot{n}_{MnF}$ . As per the reported  
392 trends,  $\dot{Q}_{TC}$  decreases by 116.7 kW, 228.7 kW, 306.9 kW, 374.5 kW, and 431.5 kW at  $\dot{n}_{inert}/\dot{n}_{ZnF}$   
393 equal to 10, 30, 40, 50, and 90, respectively, due to the increment in  $\varepsilon_{gg}$  from 0.0 to 0.9. It is  
394 also understood that the enhancement in  $\varepsilon_{gg}$  from 0.0 to 0.9 is responsible for the reduction  
395 in the difference between  $\dot{Q}_{TC}$  at  $\dot{n}_{inert}/\dot{n}_{MnF}$  equal to 10 and 100. For example, the difference  
396 between  $\dot{Q}_{TC}$  at  $\dot{n}_{inert}/\dot{n}_{MnF}$  equal to 10 and 100 decreases from 363.3 kW (at  $\varepsilon_{gg} = 0.0$ ) to  
397 172.1 kW (at  $\varepsilon_{gg} = 0.5$ ) and 19.2 kW (at  $\varepsilon_{gg} = 0.9$ ).

398 Table 3 shows the effect of  $\varepsilon_{gg}$  on  $\dot{Q}_{solar}$  for all  $\dot{n}_{inert}/\dot{n}_{MnF}$  values. Similar to  $\dot{Q}_{TC}$ ,  $\dot{Q}_{solar}$   
399 also decreases as a function of  $\varepsilon_{gg}$ . Even though there is no influence of  $\varepsilon_{gg}$  on  $\eta_{absorption}$ ,  
400 the increment in  $\varepsilon_{gg}$  from 0.0 to 0.9 is responsible for lessening  $\dot{Q}_{solar}$  by 126.0 kW, 243.5 kW,

401 324.8 kW, 394.9 kW, and 453.8 kW at  $\dot{n}_{inert}/\dot{n}_{MnF}$  equal to 10, 30, 50, 70, and 90, respectively.

402 Alike  $\dot{Q}_{TC}$ , the increase in  $\varepsilon_{gg}$  also helps to decline the difference between  $\dot{Q}_{solar}$  at

403  $\dot{n}_{inert}/\dot{n}_{MnF}$  equal to 10 and 100. For example, the difference between  $\dot{Q}_{solar}$  at  $\dot{n}_{inert}/\dot{n}_{MnF}$

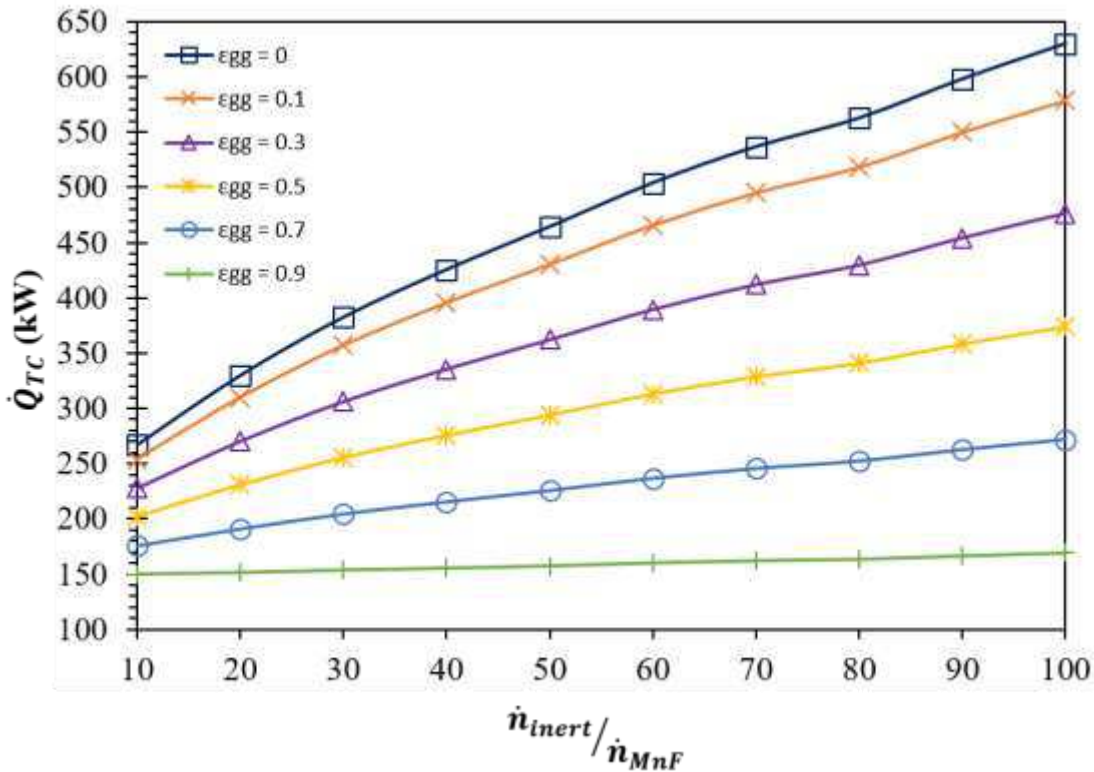
404 equal to 10 and 100 decreases from 374.1 kW to 334.3 kW, 254.7 kW, 175.1 kW, 95.5 kW, and

405 15.9 kW due to the upsurge in  $\varepsilon_{gg}$  from 0.0 to 0.1, 0.3, 0.5, 0.7, and 0.9, respectively. Similar

406 to  $\dot{Q}_{solar}$ ,  $\dot{Q}_{re-rad}$  also drops considerably when  $\varepsilon_{gg}$  increases. In terms of numbers, the

407 increment in  $\varepsilon_{gg}$  from 0.0 to 0.9 is responsible for a reduction in  $\dot{Q}_{re-rad}$  by 9.3 kW, 14.8 kW,

408 17.8 kW, 20.4 kW, and 22.3 kW at  $\dot{n}_{inert}/\dot{n}_{MnF}$  equal to 10, 30, 50, 70, and 90, respectively.



409

410 Fig. 10. Effect of  $\dot{n}_{inert}/\dot{n}_{MnF}$  and gas-to-gas heat recovery effectiveness ( $\varepsilon_{gg}$ ) on thermal

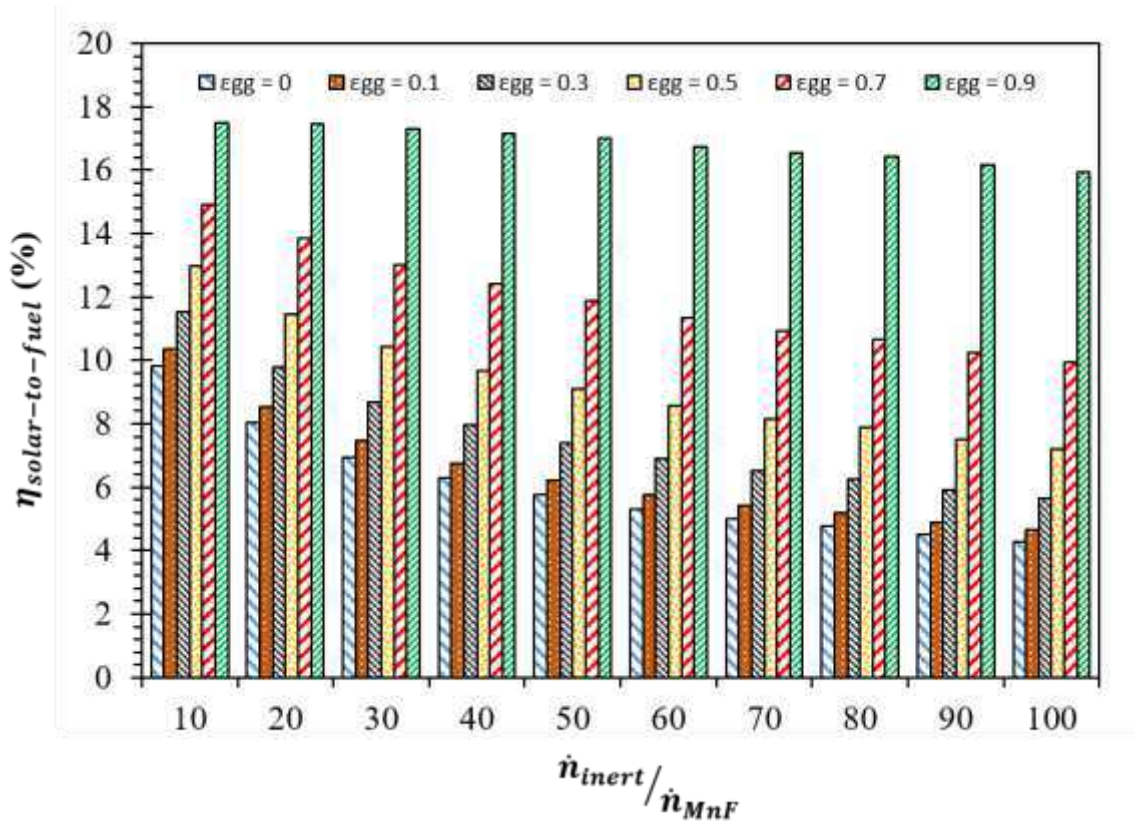
411 energy required to drive  $MnFe_2O_4$  based  $CO_2$  splitting cycle ( $\dot{Q}_{TC}$ ).

412 Table 3. Effect of  $\dot{n}_{inert}/\dot{n}_{MnF}$  and gas-to-gas heat recovery effectiveness ( $\epsilon_{gg}$ ) on the solar  
 413 energy required to operate  $MnFe_2O_4$  based  $CO_2$  splitting cycle ( $\dot{Q}_{solar}$ ).

$\dot{n}_{inert}/\dot{n}_{MnF}$	$T_{red}$ (K)	$\dot{Q}_{solar}$ (kW)					
		$\epsilon_{gg} =$ <b>0.0</b>	$\epsilon_{gg} =$ <b>0.1</b>	$\epsilon_{gg} =$ <b>0.3</b>	$\epsilon_{gg} =$ <b>0.5</b>	$\epsilon_{gg} =$ <b>0.7</b>	$\epsilon_{gg} =$ <b>0.9</b>
10	1405	288.0	274.0	246.0	218.0	190.0	162.0
20	1365	352.7	331.6	289.2	246.9	204.5	162.2
30	1340	407.2	380.2	326.1	272.0	217.8	163.7
40	1320	451.5	419.7	356.0	292.3	228.7	165.0
50	1305	491.4	455.3	383.1	311.0	238.8	166.6
60	1295	532.4	492.0	411.3	330.6	250.0	169.3
70	1285	566.0	522.1	434.4	346.6	258.9	171.1
80	1275	592.3	545.6	452.3	358.9	265.6	172.2
90	1270	629.0	578.6	477.8	376.9	276.1	175.2
100	1265	662.1	608.3	500.7	393.1	285.5	177.9

414  
 415 Due to the significant decrease in  $\dot{Q}_{solar}$ ,  $\dot{Q}_{TC}$ , and  $\dot{Q}_{re-rad}$ ,  $\eta_{solar-to-fuel}$  of  $MnFe_2O_4$   
 416 based CDS cycle increases when  $\epsilon_{gg}$  enhances from 0.0 to 0.9. The trends reported in Fig. 11  
 417 shows that as  $\epsilon_{gg}$  increments from 0.0 to 0.9,  $\eta_{solar-to-fuel}$  improves from 9.8% to 17.5%,  
 418 5.8% to 17.0%, and 4.3% to 15.9% at  $\dot{n}_{inert}/\dot{n}_{MnF}$  equal to 10, 50, and 90, respectively. It is  
 419 also understood that when the  $\dot{n}_{inert}/\dot{n}_{MnF}$  increases from 10 to 100, the drop in  $\eta_{solar-to-fuel}$   
 420 is in the range of 5% to 6% for  $\epsilon_{gg}$  equal to 0.1 to 0.7. However, in the case of  $\epsilon_{gg} = 0.9$ , as

421  $\dot{Q}_{solar}$  ranges from 162.0 kW to 177.9 kW,  $\eta_{solar-to-fuel}$  decreases by a lower amount (1.6%)  
 422 when  $\dot{n}_{inert}/\dot{n}_{MnF}$  enhances from 10 to 100. In the end, by applying  $\varepsilon_{gg} = 0.9$ , maximum  
 423  $\eta_{solar-to-fuel}$  of 17.5% can be achieved by using  $\dot{n}_{inert}/\dot{n}_{MnF}$  equal to 10 as well as 20.



424

425 Fig. 11. Effect of  $\dot{n}_{inert}/\dot{n}_{ZnF}$  and gas-to-gas heat recovery effectiveness ( $\varepsilon_{gg}$ ) on solar-to-fuel  
 426 energy conversion efficiency ( $\eta_{solar-to-fuel}$ ).

427

428

429

430

#### 431 4. Summary and Conclusions

432 A thermodynamic model for a high-temperature solar thermochemical CDS cycle driven  
433 by  $MnFe_2O_4$  is developed and used for the estimation of thermodynamics process parameters.

434 An increase in  $\dot{n}_{inert}/\dot{n}_{MnF}$  from 10 to 100 is responsible for the decrease in  $T_{red}$  from 1405 K to

435 1265 K. The initial calculations which are performed at  $\varepsilon_{gg} = 0.7$  confirms a slight enhancement

436 in  $\dot{Q}_{MnF-red}$  (0.4 kW) even though the  $T_{red}$  reduces by 140 K. Conversely,  $\dot{Q}_{MnF-sens}$  decreases

437 by 26.9 kW due to the drop in  $T_{red}$  from 1405 K to 1265 K. The amount of heat energy required

438 for the separation of inert from the inert/O<sub>2</sub> gas mixture increases by 7.2 kW as  $\dot{n}_{inert}/\dot{n}_{MnF}$

439 enhances from 10 to 100. Opposite to this, due to the unchanged molar flow rates of CO<sub>2</sub> and

440 CO, the heat energy needed to separate CO from CO<sub>2</sub>/CO gas mixture remains steady. The rise in

441  $\dot{n}_{inert}/\dot{n}_{MnF}$  from 10 to 100 is also responsible for the increase in  $\dot{Q}_{heater-1}$  from 24.9 kW to

442 139.9 kW, respectively. This rise in the thermal energy required for the heating of inert sweep

443 gas results in an enhancement in  $\dot{Q}_{solar}$  from 190.0 kW to 285.5 kW, which further decreases

444  $\eta_{solar-to-fuel}$  by ~5%. To improve the  $\eta_{solar-to-fuel}$ ,  $\varepsilon_{gg}$  is enhanced from 0.7 to 0.9, which

445 significantly reduces  $\dot{Q}_{TC}$  and  $\dot{Q}_{solar}$ . At  $\varepsilon_{gg}$  equal to 0.9,  $\dot{Q}_{TC}$  and  $\dot{Q}_{solar}$  attains lowest values,

446 i.e., 150.1 kW and 162.0 kW (at  $\dot{n}_{inert}/\dot{n}_{MnF} = 10$ ). The reduction in both  $\dot{Q}_{TC}$  and  $\dot{Q}_{solar}$  helps

447  $MnFe_2O_4$  based CDC cycle to accomplish  $\eta_{solar-to-fuel}$  equal to 17.5%.

#### 448 Acknowledgments

449 The author would like to thank Qatar University for its support.

450

451 **Declarations**

452 **Funding:** The author would like to thank Qatar University for its support

453 **Conflicts of interest/Competing interests:** No conflicts of interest/competing interests

454 **Availability of data and material:** Not applicable

455 **Code availability :** Not applicable

456 **Authors' contributions :** A single author paper

457 **Ethics approval :** Not applicable

458 **Consent to participate:** Not applicable

459 **Consent for publication:** Not applicable

460

461

462

463

464

465

466

467

468

469 **Nomenclature**

470	$C$	Solar flux concentration ratio, suns
471	$HHV_{CO}$	Higher heating value of CO, kW
472	HEX-1	Heat exchanger-1
473	HEX-2	Heat exchanger-2
474	HEX-3	Heat exchanger-3
475	HEX-4	Heat exchanger-4
476	HEX-5	Heat exchanger-5
477	$I$	Normal beam solar insolation, W/m <sup>2</sup>
478	$MO$	Metal oxide
479	$n$	Molar amount, mol
480	$n_{CO,oxd_3}$	Molar amount of CO at state $oxd_3$ , mol
481	$n_{CO,oxd_4}$	Molar amount of CO at state $oxd_4$ , mol
482	$n_{O_2,red_1}$	Molar amount of O <sub>2</sub> at state $red_1$ , mol
483	$n_{O_2,red_2}$	Molar amount of O <sub>2</sub> at state $red_2$ , mol
484	$\dot{n}$	Molar flow rate, mol/s
485	$\dot{n}_{inert}$	Molar flow rate of inert, mol/s
486	$\dot{n}_{MnF}$	Molar flow rate of $MnFe_2O_4$ , mol/s
487	$\dot{n}_{inert}/\dot{n}_{MnF}$	Ratio of molar flow rates of inert to $MnFe_2O_4$
488	$\dot{n}_{CO_2}$	Molar flow rate of CO <sub>2</sub> , mol/s
489	$\dot{n}_{CO}$	Molar flow rate of CO, mol/s

490	$\dot{n}_{O_2}$	Molar flow rate of O <sub>2</sub> , mol/s
491	$\dot{Q}_{inert-heat}$	Thermal energy required to heat inert sweep gas, kW
492	$\dot{Q}_{(inert+O_2)-cool}$	Thermal energy released during cooling of inert + O <sub>2</sub> gas mixture, kW
493	$\dot{Q}_{(CO_2+CO)-cool}$	Thermal energy released during cooling of CO <sub>2</sub> + CO gas mixture, kW
494	$\dot{Q}_{CO_2-cool}$	Thermal energy released during cooling of CO <sub>2</sub> , kW
495	$\dot{Q}_{CO_2-heat}$	Thermal energy required to heat CO <sub>2</sub> , kW
496	$\dot{Q}_{heater-1}$	Auxiliary thermal energy required to heat inert sweep gas, kW
497	$\dot{Q}_{heater-2}$	Auxiliary thermal energy required to heat CO <sub>2</sub> , kW
498	$\dot{Q}_{O_2-cool}$	Thermal energy released during cooling of O <sub>2</sub> , kW
499	$\dot{Q}_{solar}$	Solar energy required to run the cycle, kW
500	$\dot{Q}_{sep-1}$	Thermal energy required for the operation of separator-1, kW
501	$\dot{Q}_{sep-2}$	Thermal energy required for the operation of separator-2, kW
502	$\dot{Q}_{surf}$	Thermal energy losses over the reduction chamber walls, kW
503	$\dot{Q}_{TC}$	Thermal energy required to run the cycle, Kw
504	$\dot{Q}_{MnF-red}$	Thermal energy required for thermal reduction of $MnFe_2O_4$ , kW
505	$\dot{Q}_{MnF-sens}$	Thermal energy required to heat the $MnFe_2O_4$ , kW
506	$\dot{Q}_{MnF-oxd}$	Thermal energy released during re-oxidation of $MnFe_2O_4$ , kW
507	$\dot{Q}_{re-rad}$	Re-radiation losses from the cycle, kW

508	$R$	Ideal gas constant (8.314 J/mol·K)
509	$T_0$	Ambient temperature, K
510	$T_{oxd}$	Oxidation (splitting) temperature, K
511	$T_{red}$	Reduction temperature, K
512	$T_{sep-1}$	Operating temperature of separator-1, K
513	$T_{sep-2}$	Operating temperature of separator-2, K
514	$y_{CO,oxd_3}$	Mol fraction of CO at state $oxd_3$ , mol
515	$y_{CO,oxd_4}$	Mol fraction of CO at state $oxd_4$ , mol
516	$y_{O_2,red_1}$	Mol fraction of O <sub>2</sub> at state $red_1$ , mol
517	$y_{O_2,red_2}$	Mol fraction of O <sub>2</sub> at state $red_2$ , mol
518	$\eta_{absorption}$	Solar energy absorption efficiency, %
519	$\eta_{sep-1}$	Efficiency of separator-1, %
520	$\eta_{sep-2}$	Efficiency of separator-2, %
521	$\eta_{solar-to-fuel}$	Solar-to-fuel energy conversion efficiency, %
522	$\delta_{red}$	Reduction nonstoichiometry
523	$\varepsilon_{gg}$	Gas-to-gas heat recovery effectiveness

524  $\epsilon_{SS}$  Solid-to-solid heat recovery effectiveness

525  $\sigma$  Stefan – Boltzmann constant,  $5.670 \times 10^{-8}$  (W/m<sup>2</sup>·K<sup>4</sup>)

526

527

528

529

530

531

532

533

534

535

536

537

538

539 **References**

- 540 Abanades S, Charvin P, Lemont F, Flamant G (2008) Novel two-step SnO<sub>2</sub>/SnO water-splitting  
541 cycle for solar thermochemical production of hydrogen. *Int J Hydrogen Energy* 33:6021–  
542 6030. <https://doi.org/10.1016/j.ijhydene.2008.05.042>
- 543 Agrafiotis C, Roeb M, Sattler C (2015) A review on solar thermal syngas production via redox  
544 pair-based water/carbon dioxide splitting thermochemical cycles. *Renew. Sustain. Energy*  
545 *Rev.* 42:254–285
- 546 Alvani C, Ennas G, La Barbera A, et al (2005) Synthesis and characterization of nanocrystalline  
547 MnFe<sub>2</sub>O<sub>4</sub>: Advances in thermochemical water splitting. *Int J Hydrogen Energy* 30:1407–  
548 1411. <https://doi.org/10.1016/j.ijhydene.2004.10.020>
- 549 Amar VS, Puszynski JA, Shende R V. (2015) H<sub>2</sub> generation from thermochemical water-splitting  
550 using yttria stabilized NiFe<sub>2</sub>O<sub>4</sub> core-shell nanoparticles. *J Renew Sustain Energy* 7:.  
551 <https://doi.org/10.1063/1.4915312>
- 552 Anderson LL, Armstrong PA, Broekhuis RR, et al (2016) Advances in ion transport membrane  
553 technology for oxygen and syngas production. *Solid State Ionics* 288:331–337.  
554 <https://doi.org/10.1016/j.ssi.2015.11.010>
- 555 Bhosale R, Khadka R, Puszynski J, Shende R (2011) H<sub>2</sub> generation from two-step  
556 thermochemical water-splitting reaction using sol-gel derived Sn<sub>x</sub>Fe<sub>y</sub>O<sub>z</sub>. *J Renew Sustain*  
557 *Energy*. <https://doi.org/10.1063/1.3659684>
- 558 Bhosale RR (2019a) Thermodynamic analysis of Ni-ferrite based solar thermochemical H<sub>2</sub> O

559 splitting cycle for H<sub>2</sub> production. *Int J Hydrogen Energy* 61–71.  
560 <https://doi.org/10.1016/j.ijhydene.2018.03.145>

561 Bhosale RR (2019b) Mn-ferrite based solar thermochemical water splitting cycle: A  
562 thermodynamic evaluation. *Fuel* 256:. <https://doi.org/10.1016/j.fuel.2019.115847>

563 Bhosale RR, Shende R V., Puszynski JA (2012) Thermochemical water-splitting for H<sub>2</sub>  
564 generation using sol-gel derived Mn-ferrite in a packed bed reactor. In: *International*  
565 *Journal of Hydrogen Energy*. pp 2924–2934

566 Bhosale RR, Takalkar G, Sutar P, et al (2019) A decade of ceria based solar thermochemical  
567 H<sub>2</sub>O/CO<sub>2</sub> splitting cycle. *Int J Hydrogen Energy* 34–60.  
568 <https://doi.org/10.1016/j.ijhydene.2018.04.080>

569 Bulfin B, Call F, Lange M, et al (2015) Thermodynamics of CeO<sub>2</sub> thermochemical fuel  
570 production. *Energy and Fuels* 29:1001–1009. <https://doi.org/10.1021/ef5019912>

571 Carrillo RJ, Scheffe JR (2019) Beyond Ceria: Theoretical Investigation of Isothermal and Near-  
572 Isothermal Redox Cycling of Perovskites for Solar Thermochemical Fuel Production. *Energy*  
573 *and Fuels*. <https://doi.org/10.1021/acs.energyfuels.9b02714>

574 Dey S, Naidu BS, Rao CNR (2015) Ln<sub>0.5</sub>A<sub>0.5</sub>MnO<sub>3</sub> (Ln=Lanthanide, A= Ca, Sr) perovskites  
575 exhibiting remarkable performance in the thermochemical generation of CO and H<sub>2</sub> from  
576 CO<sub>2</sub> and H<sub>2</sub>O. *Chem - A Eur J* 21:7077–7081. <https://doi.org/10.1002/chem.201500442>

577 Dry ME (2002) The Fischer-Tropsch process: 1950-2000. In: *Catalysis Today*. pp 227–241

578 Ehrensberger K, Kuhn P, Shklover V, Oswald HR (1996) Temporary phase segregation processes  
579 during the oxidation of  $(\text{Fe}_{0.7}\text{Mn}_{0.3})_{0.99}\text{O}$  in  $\text{N}_2\text{-H}_2\text{O}$  atmosphere. *Solid State Ionics*  
580 90:75–81. [https://doi.org/10.1016/s0167-2738\(96\)00376-1](https://doi.org/10.1016/s0167-2738(96)00376-1)

581 Ehrhart BD, Muhich CL, Al-Shankiti I, Weimer AW (2016) System efficiency for two-step metal  
582 oxide solar thermochemical hydrogen production – Part 1: Thermodynamic model and  
583 impact of oxidation kinetics. *Int J Hydrogen Energy* 41:19881–19893.  
584 <https://doi.org/10.1016/j.ijhydene.2016.07.109>

585 Fresno F, Fernández-Saavedra R, Belén Gómez-Mancebo M, et al (2009) Solar hydrogen  
586 production by two-step thermochemical cycles: Evaluation of the activity of commercial  
587 ferrites. *Int J Hydrogen Energy* 34:2918–2924.  
588 <https://doi.org/10.1016/j.ijhydene.2009.02.020>

589 Go KS, Son SR, Kim SD (2008) Reaction kinetics of reduction and oxidation of metal oxides for  
590 hydrogen production. *Int J Hydrogen Energy* 33:5986–5995.  
591 <https://doi.org/10.1016/j.ijhydene.2008.05.039>

592 Inoue M, Hasegawa N, Uehara R, et al (2004) Solar hydrogen generation with  
593  $\text{H}_2\text{O}/\text{ZnO}/\text{MnFe}_2\text{O}_4$  system. *Sol Energy* 76:309–315.  
594 <https://doi.org/10.1016/j.solener.2003.08.033>

595 Kodama T, Nakamuro Y, Mizuno T (2006) A two-step thermochemical water splitting by iron-  
596 oxide on stabilized zirconia. *J Sol Energy Eng Trans ASME* 128:3–7.  
597 <https://doi.org/10.1115/1.1878852>

598 Koepf E, Villasmil W, Meier A (2016) Pilot-scale solar reactor operation and characterization for  
599 fuel production via the Zn/ZnO thermochemical cycle. *Appl Energy* 165:1004–1023.  
600 <https://doi.org/10.1016/j.apenergy.2015.12.106>

601 Lu Y, Zhu L, Agrafiotis C, et al (2019) Solar fuels production: Two-step thermochemical cycles  
602 with cerium-based oxides. *Prog. Energy Combust. Sci.* 75

603 Padella F, Alvani C, La Barbera A, et al (2005) Mechanochemical synthesis and process characterization of  
604 nanostructured manganese ferrite. *Mater Chem Phys* 90:172–177.  
605 <https://doi.org/10.1016/j.matchemphys.2004.10.033>

606 Randhir K, Rhodes NR, Li L, et al (2018) Magnesioferrites for solar thermochemical fuel  
607 production. *Sol Energy* 163:1–15. <https://doi.org/10.1016/j.solener.2017.12.006>

608 Scheffe JR, Li J, Weimer AW (2010) A spinel ferrite/hercynite water-splitting redox cycle. *Int J*  
609 *Hydrogen Energy* 35:3333–3340. <https://doi.org/10.1016/j.ijhydene.2010.01.140>

610 Takalkar G, Bhosale RR, AlMomani F (2019) Thermochemical splitting of CO<sub>2</sub> using Co-  
611 precipitation synthesized Ce<sub>0.75</sub>Zr<sub>0.2</sub>M<sub>0.05</sub>O<sub>2-Δ</sub> (M = Cr, Mn, Fe, Co, Ni, Zn) materials.  
612 *Fuel* 256:.. <https://doi.org/10.1016/j.fuel.2019.115834>

613 Takalkar G, Bhosale RR, AlMomani F, et al (2020) Ni incorporation in MgFe<sub>2</sub>O<sub>4</sub> for improved  
614 CO<sub>2</sub>-splitting activity during solar fuel production. *J Mater Sci* 55:11086–11094.  
615 <https://doi.org/10.1007/s10853-020-04794-1>

616 Tamaura Y, Hasegawa N, Kojima M, et al (1998) Water splitting with the Mn(II)-ferrite-CaO-H<sub>2</sub>O  
617 system at 1273K. *Energy* 23:879–886. [https://doi.org/10.1016/S0360-5442\(98\)00030-9](https://doi.org/10.1016/S0360-5442(98)00030-9)

618 Tamaura Y, Kojima N, Hasegawa N, et al (2001) Stoichiometric studies of H<sub>2</sub> generation reaction  
619 for H<sub>2</sub>O/Zn/Fe<sub>3</sub>O<sub>4</sub> system. Int J Hydrogen Energy 26:917–922.  
620 [https://doi.org/10.1016/S0360-3199\(01\)00039-8](https://doi.org/10.1016/S0360-3199(01)00039-8)

621

622

623

624

625

626

627

628

629

630

631

632

633

# Figures

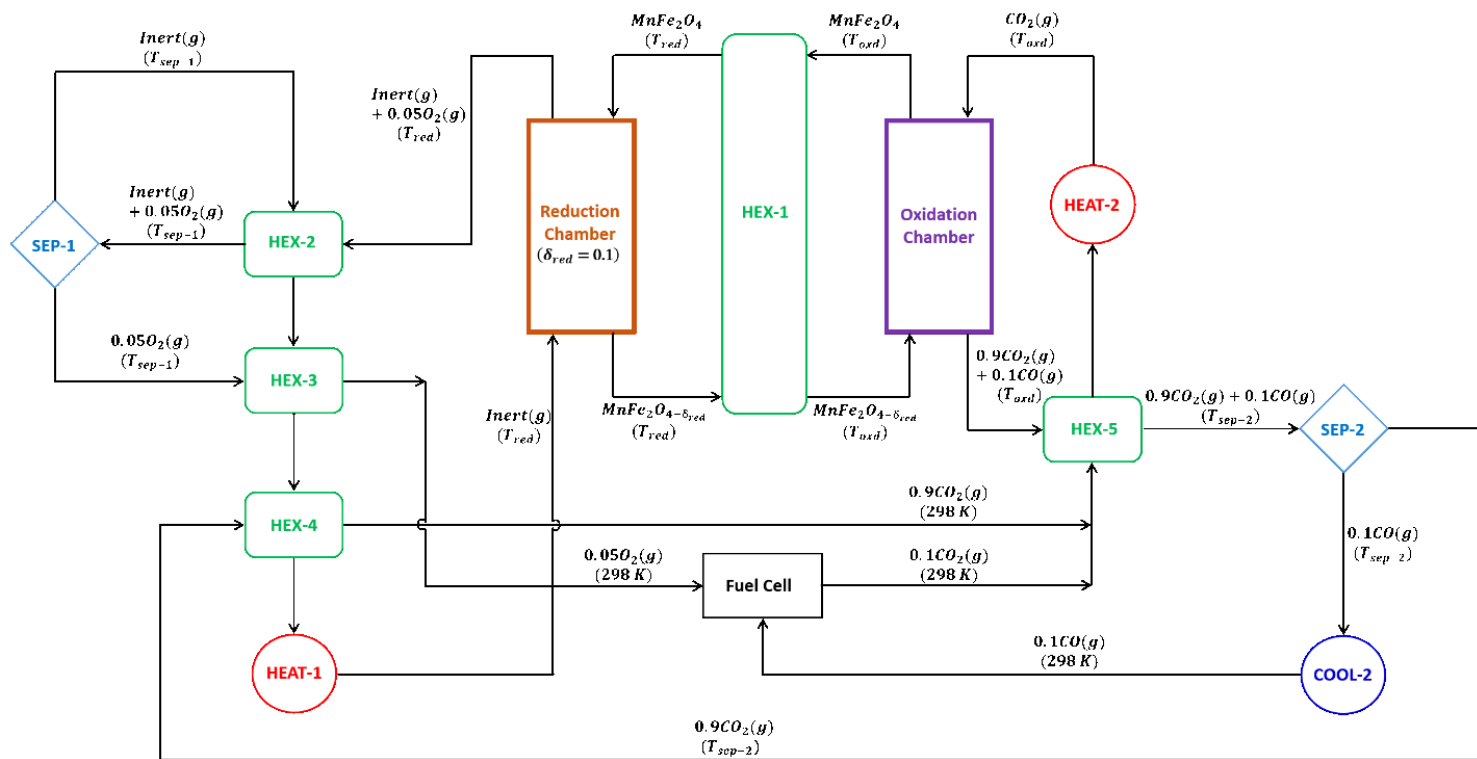


Figure 1

See the Supplemental Files section for the complete figure caption.

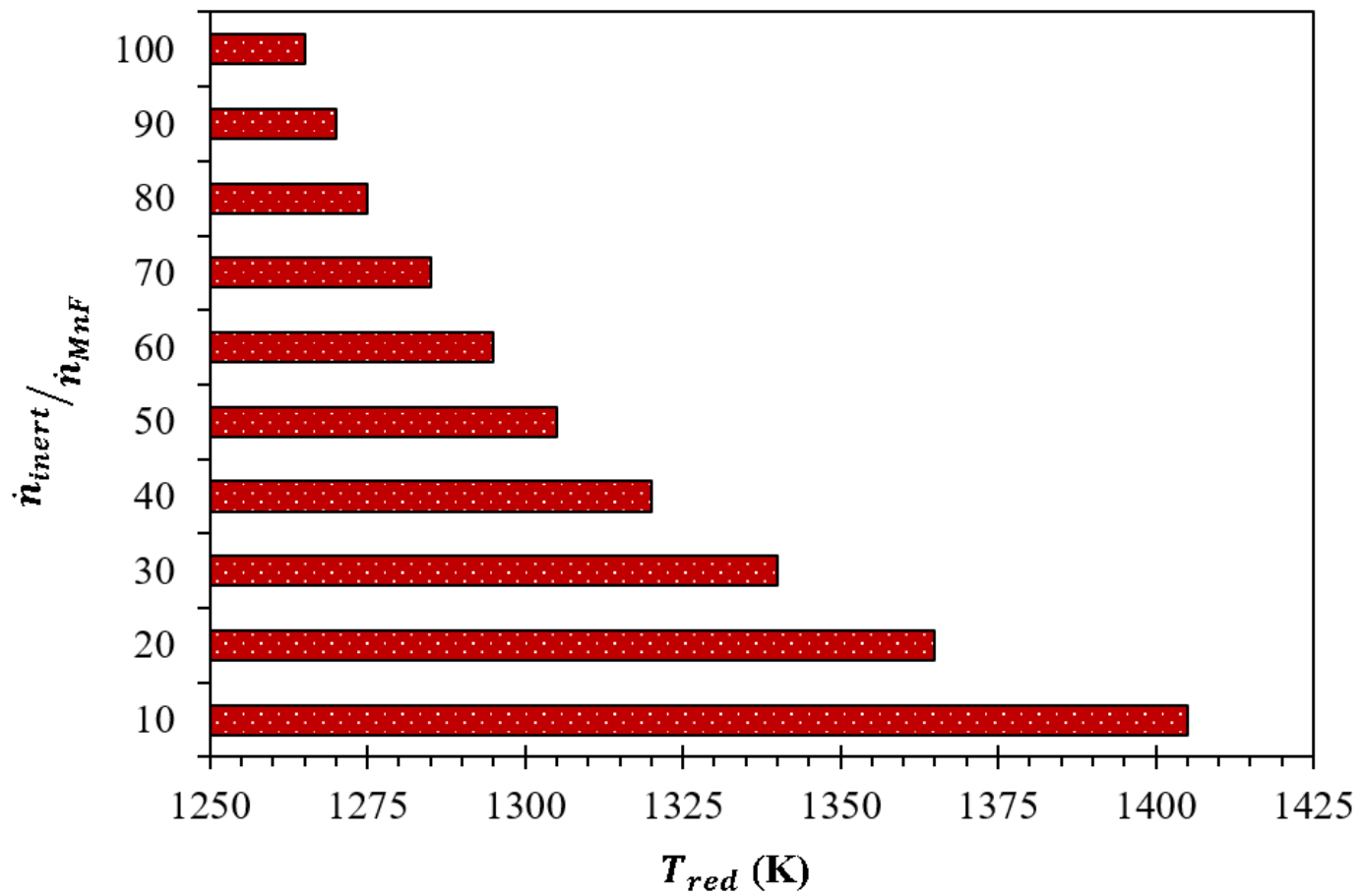


Figure 2

See the Supplemental Files section for the complete figure caption.

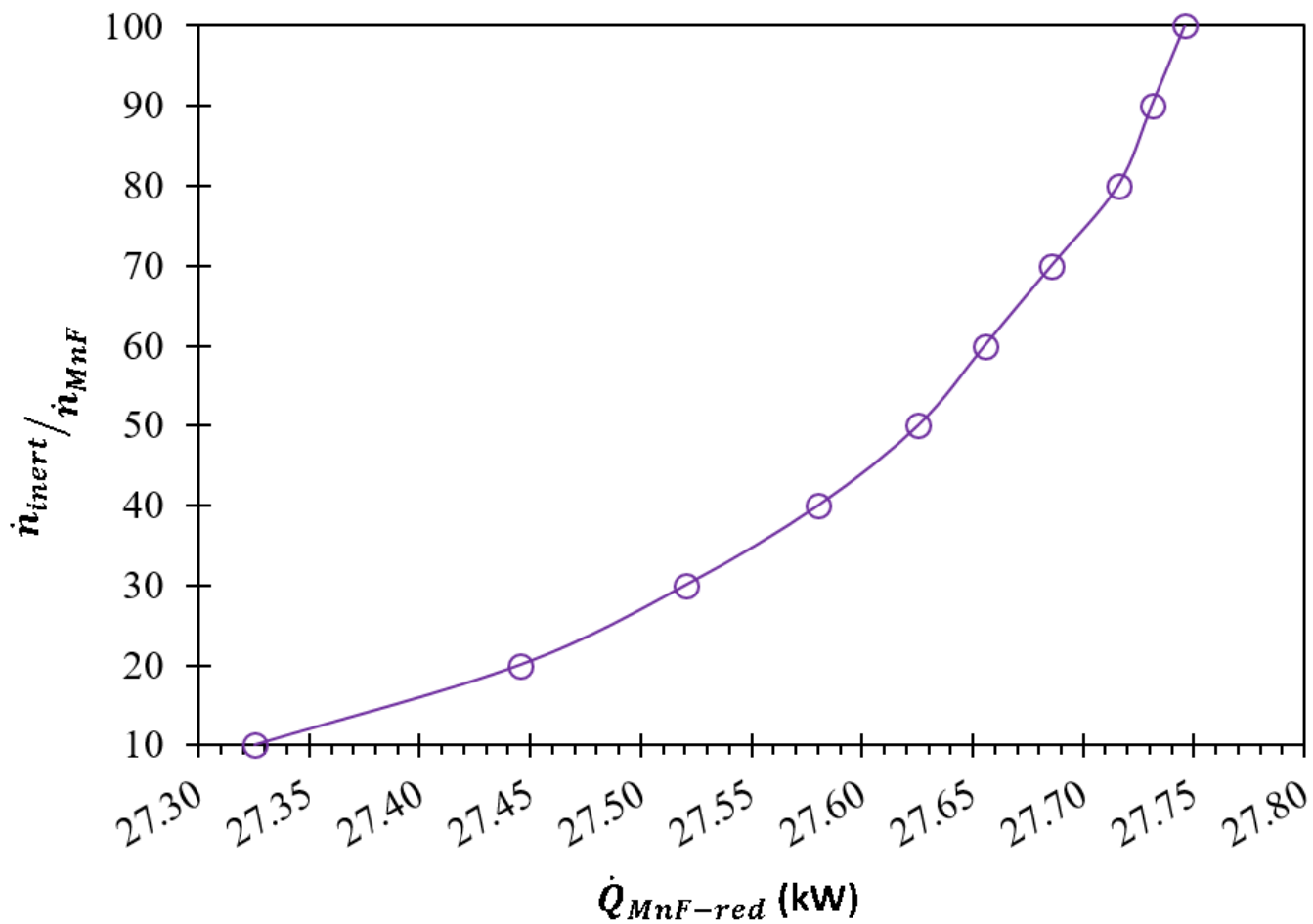


Figure 3

See the Supplemental Files section for the complete figure caption.

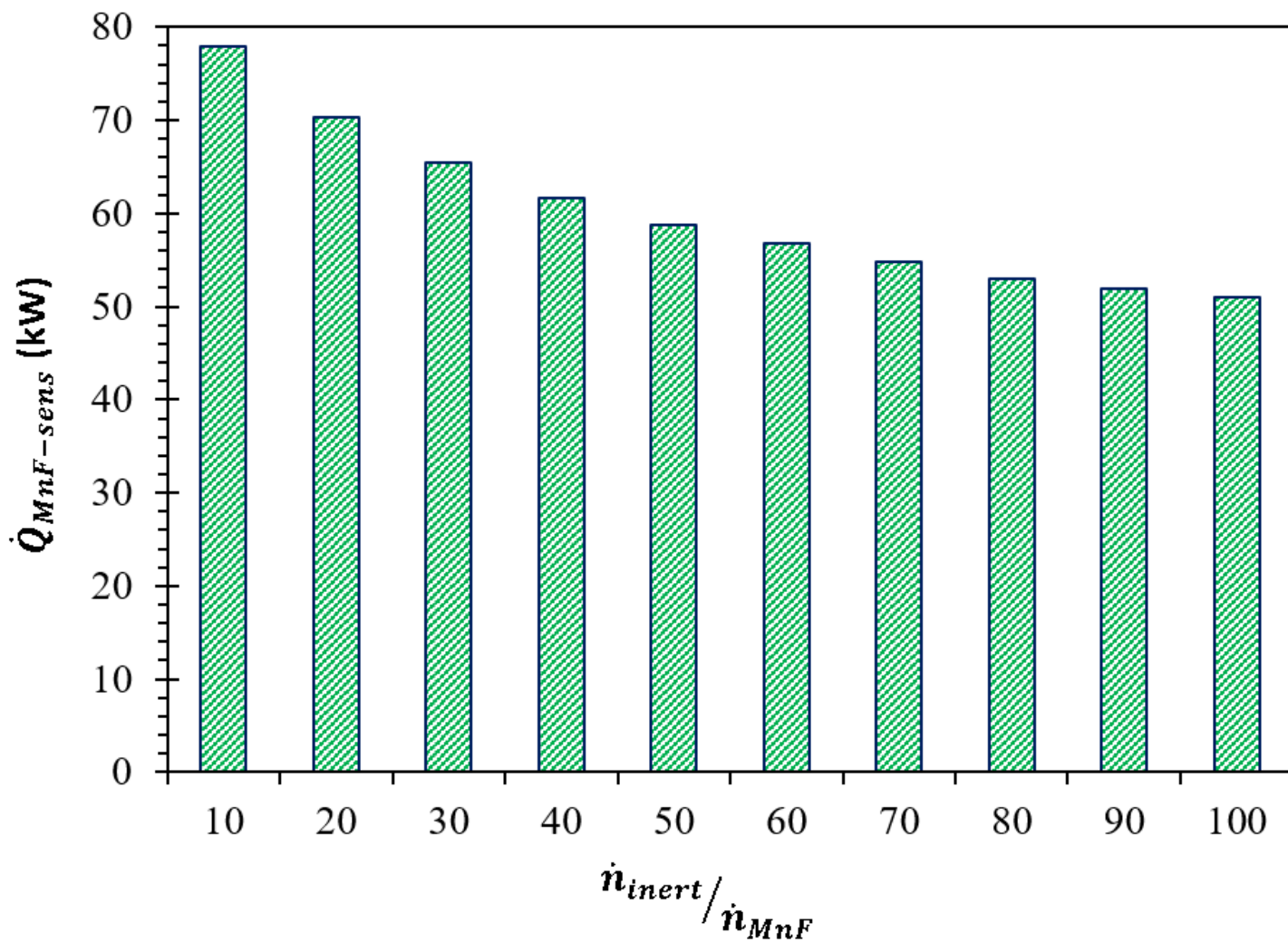


Figure 4

See the Supplemental Files section for the complete figure caption.

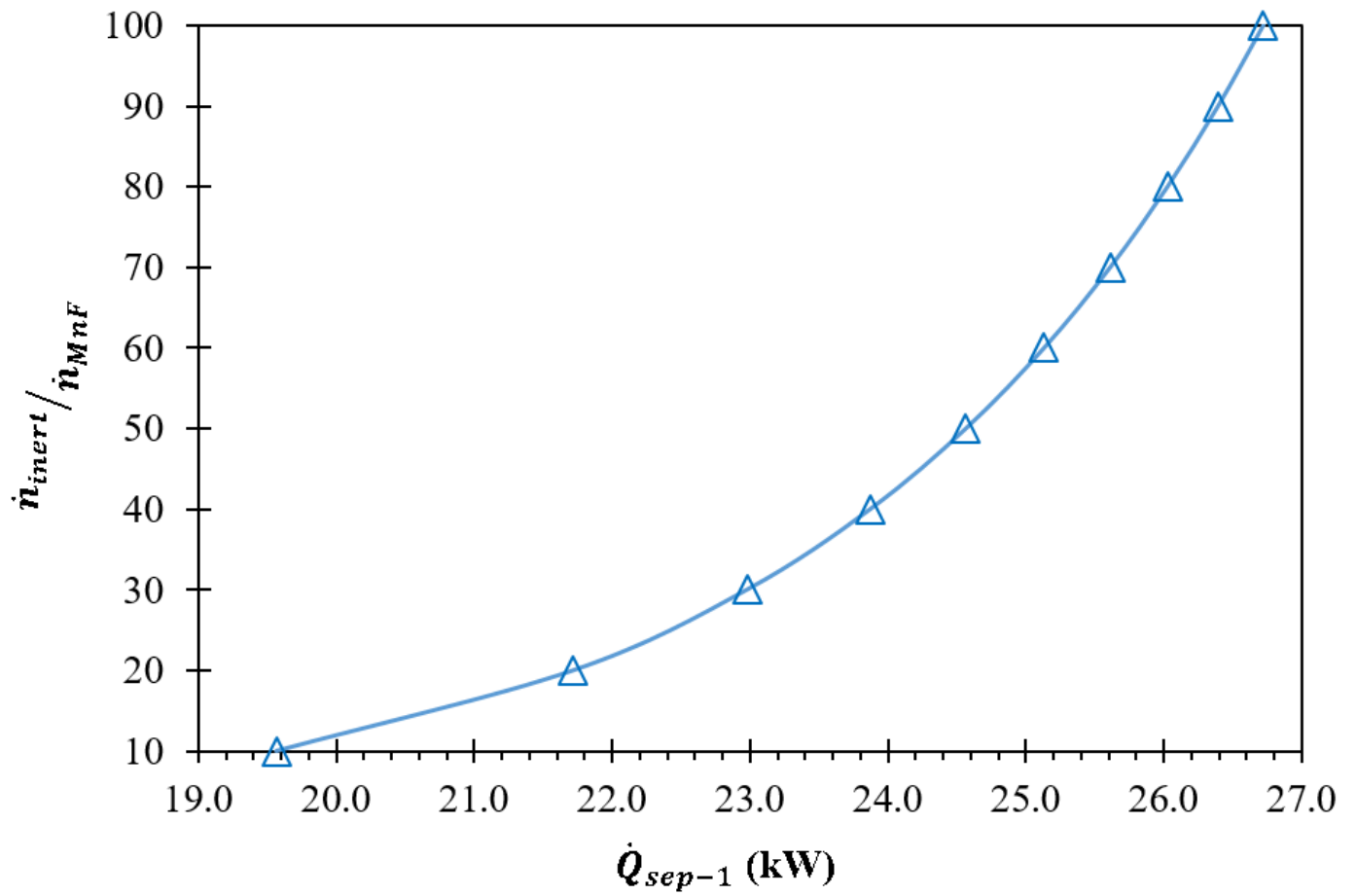


Figure 5

See the Supplemental Files section for the complete figure caption.

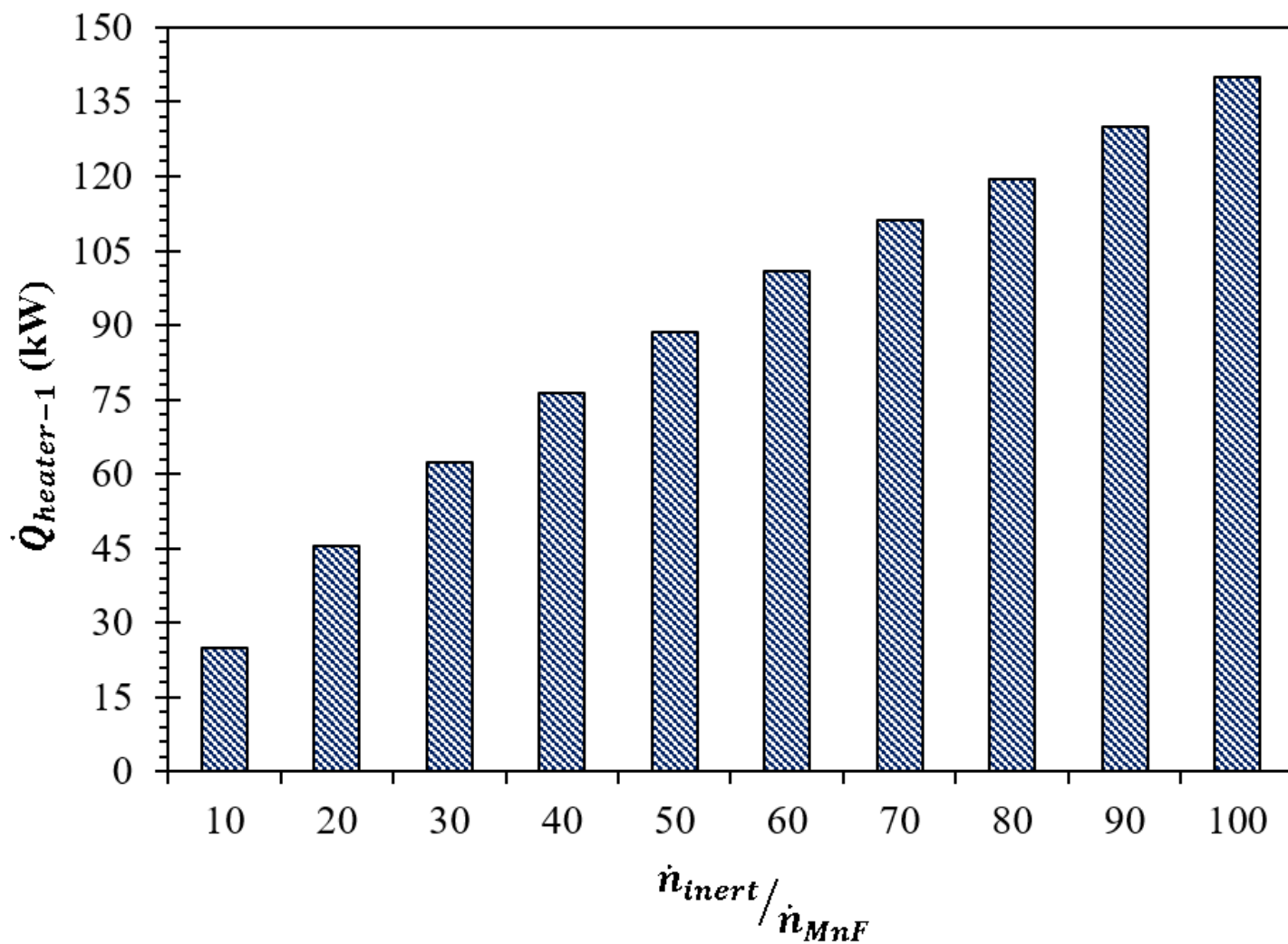


Figure 6

See the Supplemental Files section for the complete figure caption.

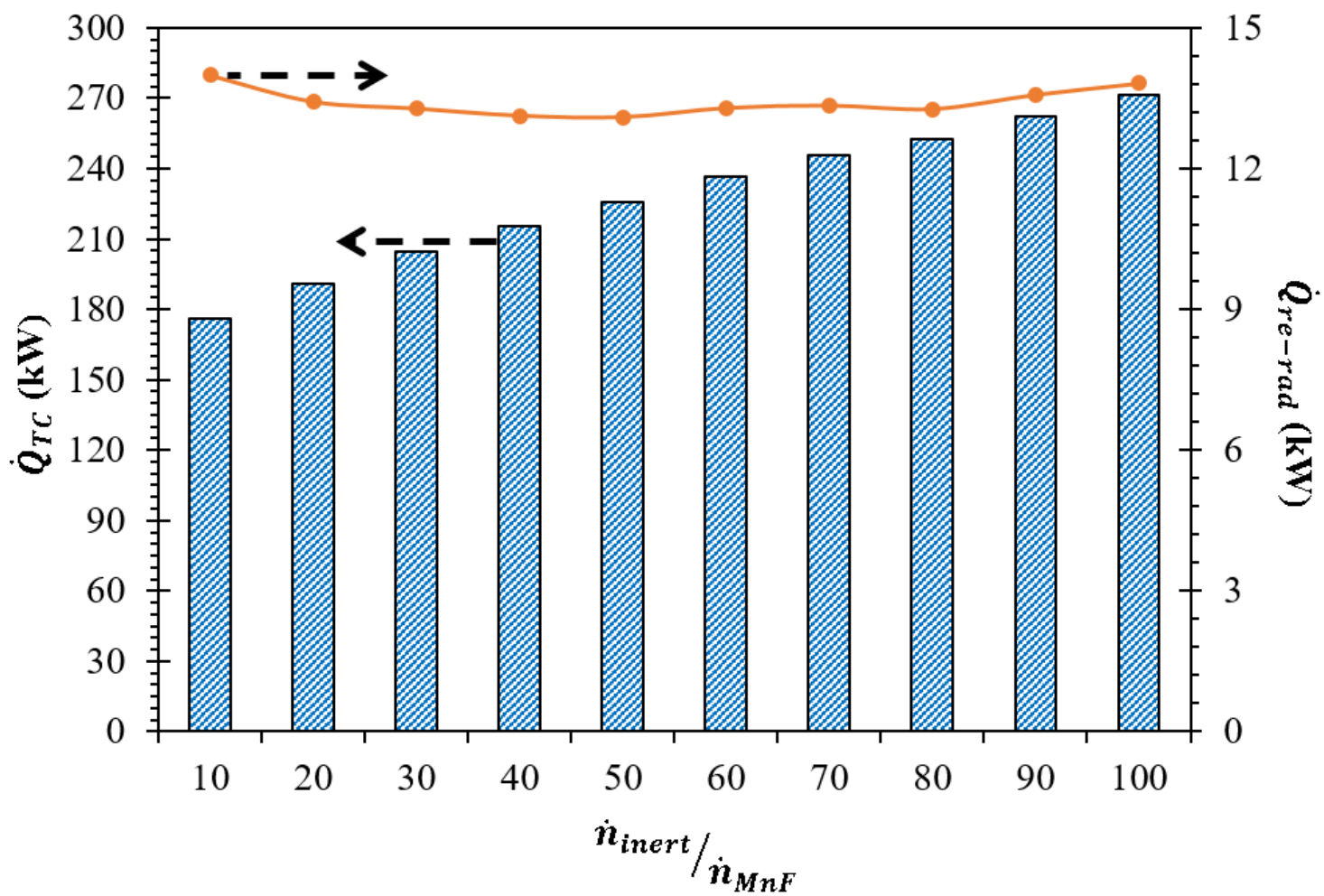


Figure 7

See the Supplemental Files section for the complete figure caption.

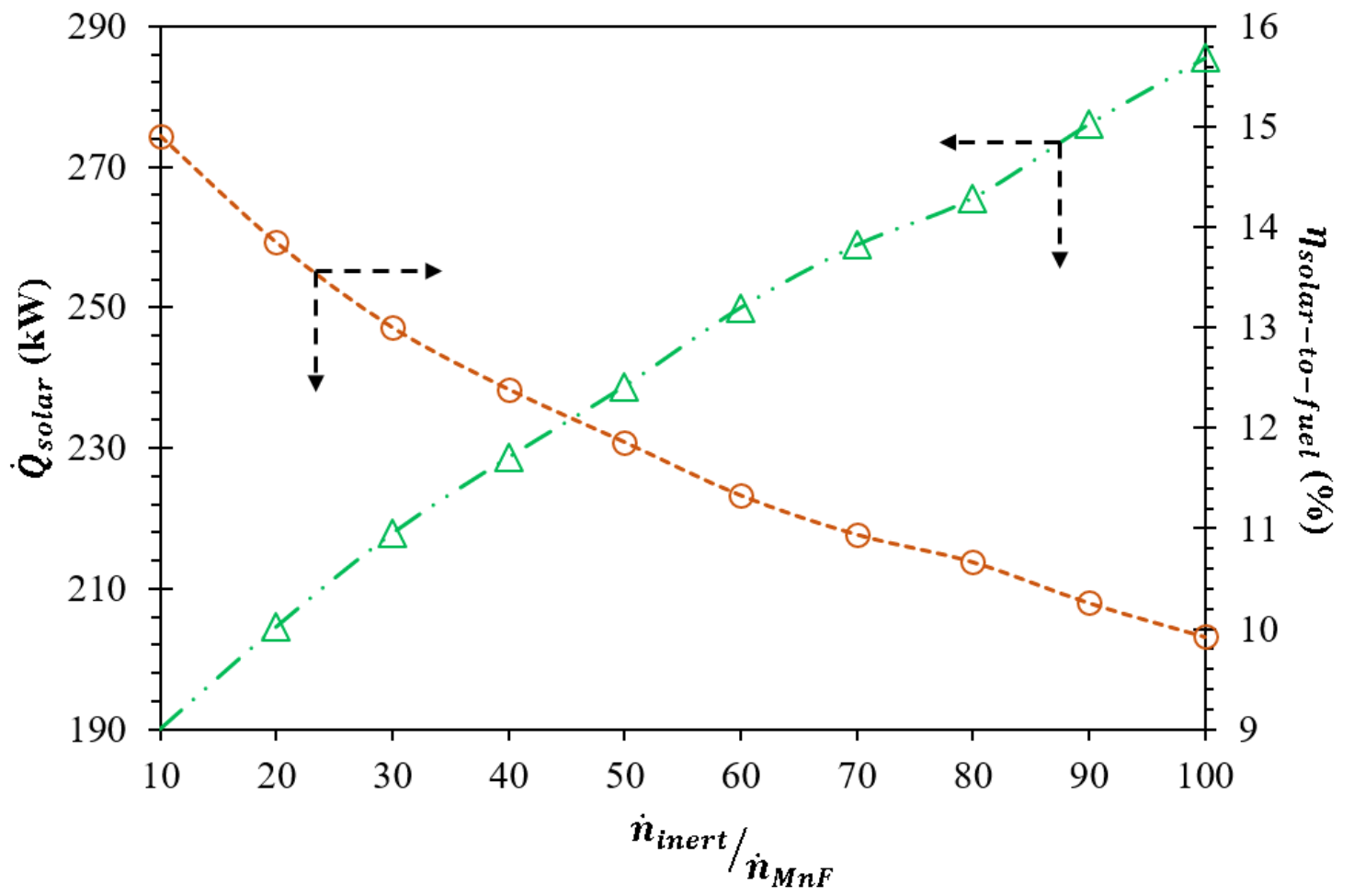


Figure 8

See the Supplemental Files section for the complete figure caption.

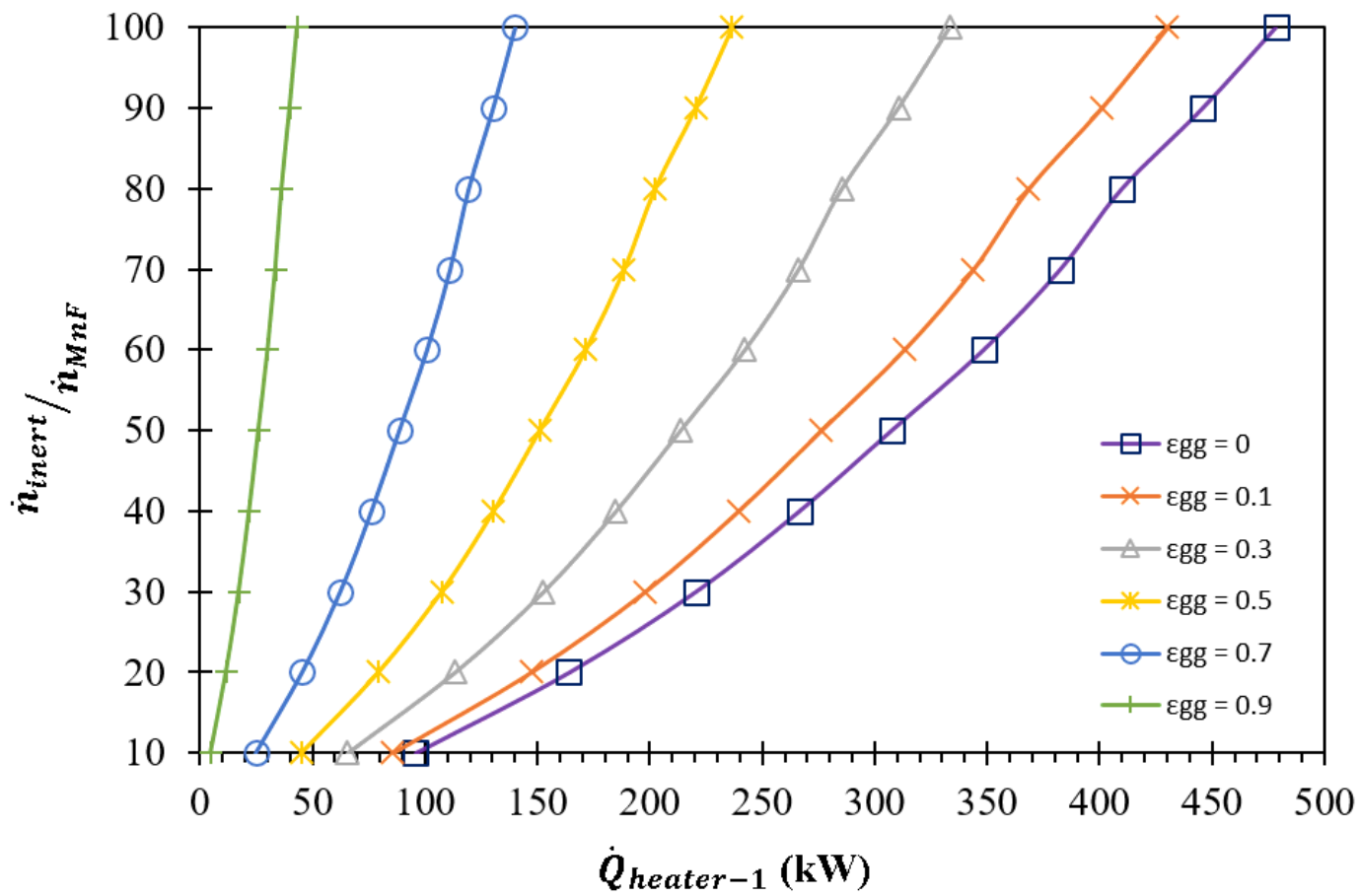


Figure 9

See the Supplemental Files section for the complete figure caption.

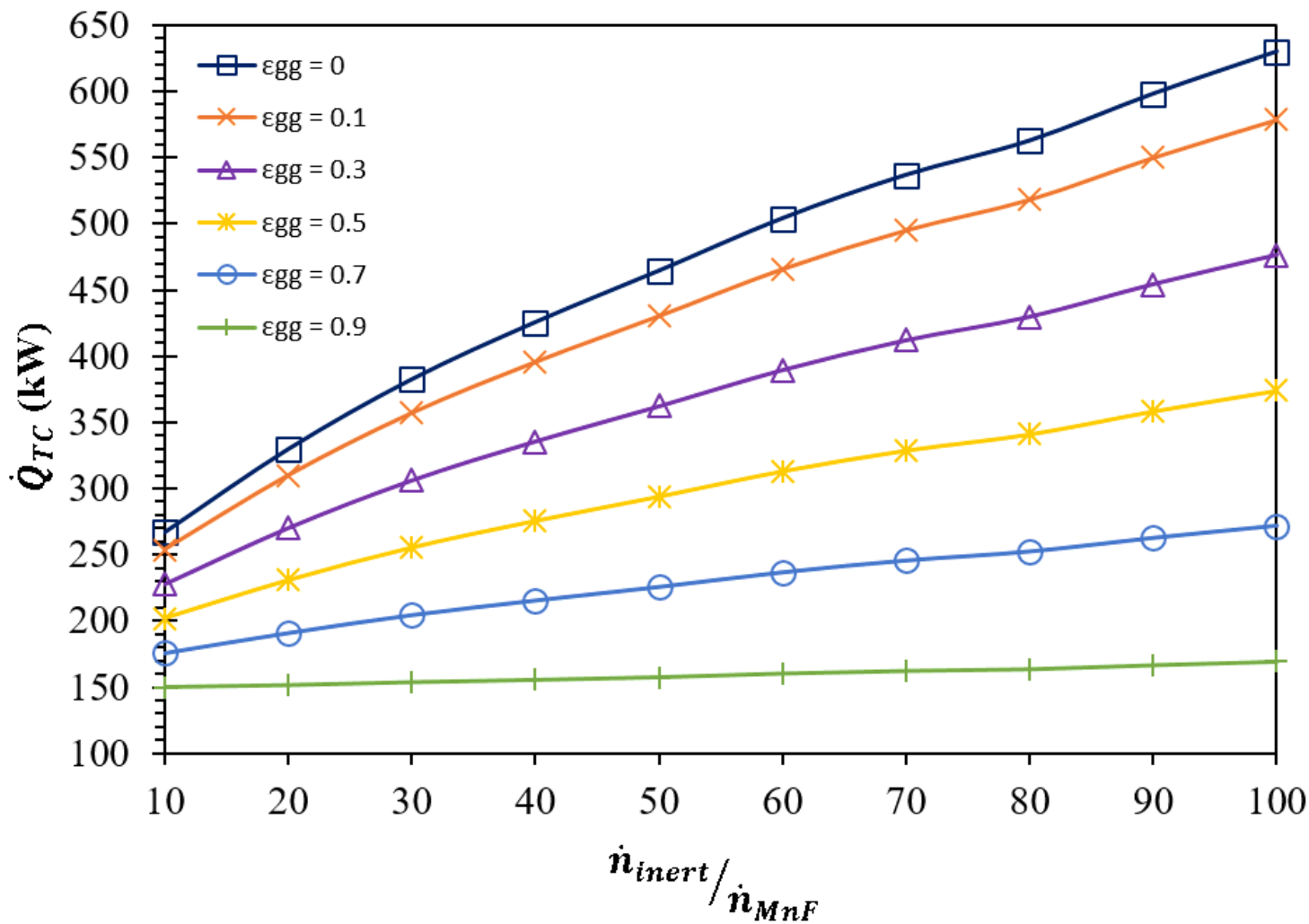


Figure 10

See the Supplemental Files section for the complete figure caption.

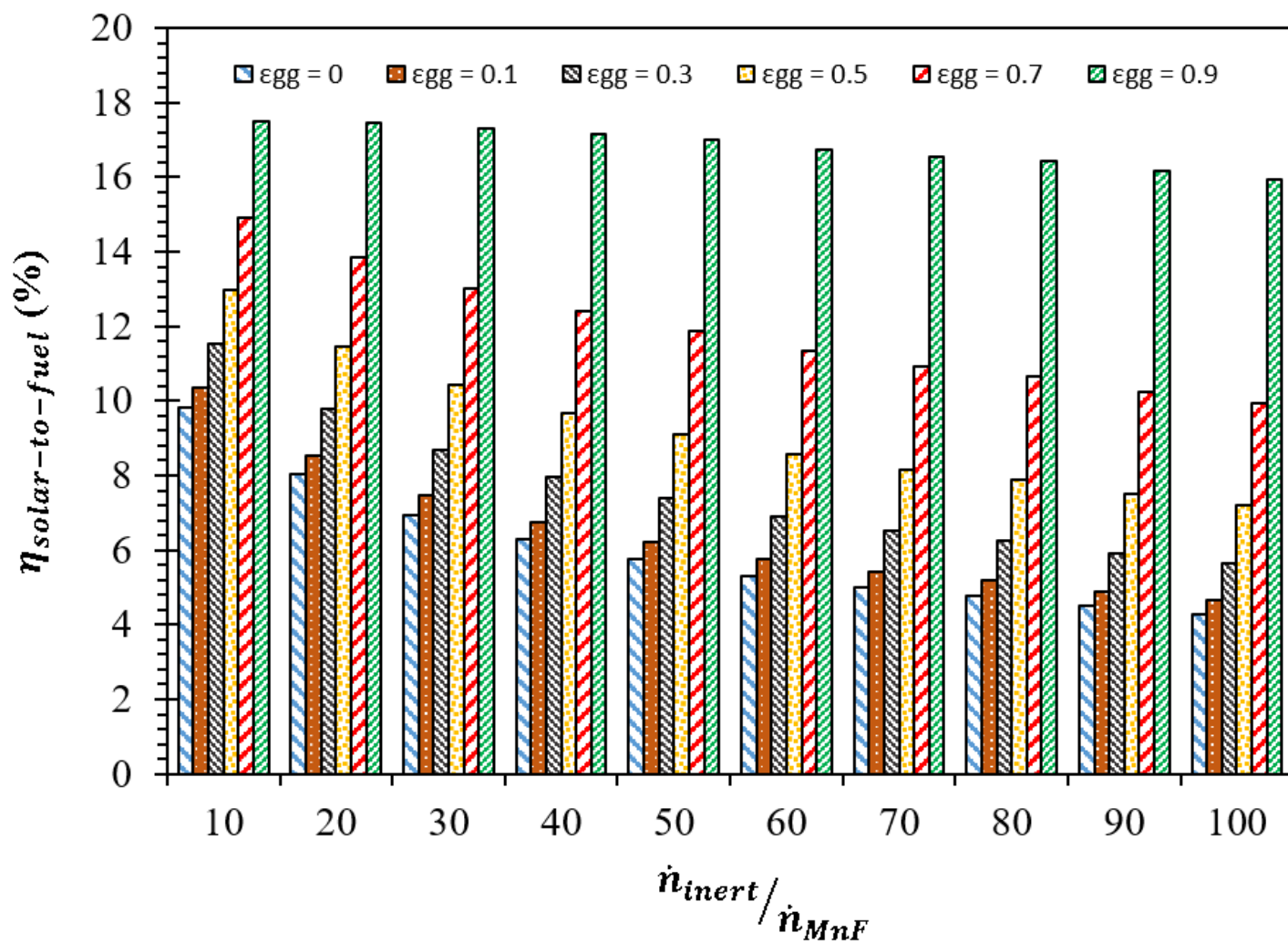


Figure 11

See the Supplemental Files section for the complete figure caption.

## Supplementary Files

This is a list of supplementary files associated with this preprint. Click to download.

- [FigureCaptions.docx](#)
- [GraphicalAbstract.docx](#)